The Astrophysical Journal, 985:51 (24pp), 2025 May 20 https://doi.org/10.3847/1538-4357/adc2fb


# Dinosaur in a Haystack: X-Ray View of the Entrails of SN 2023ixf and the Radio Afterglow of Its Interaction with the Medium Spawned by the Progenitor Star (Paper I)*

Nayana A. J.[1,30], Raffaella Margutti[1,2], Eli Wiston[1], Ryan Chornock[1], Sergio Campana[3], Tanmoy Laskar[4,5], Kohta Murase[6,7], Melanie Krips[8], Giulia Migliori[9], Daichi Tsuna[10,11], Kate D. Alexander[12], Poonam Chandra[13], Michael Bietenholz[14], Edo Berger[15], Roger A. Chevalier[16], Fabio De Colle[17], Luc Dessart[18], Rebecca Diesing[19], Brian W. Grefenstette[20], Wynn V. Jacobson-Galán[1,21,31], Keiichi Maeda[22], Benito Marcote[23,24], Daisy Matthews[25], Dan Milisavljevic[26,27], Alak K. Ray[28], Andrea Reguitti[3], and Ava Polzin[29]

[1] Department of Astronomy, University of California, Berkeley, CA 94720-3411, USA; nayana@berkeley.edu
[2] Department of Physics, University of California, 366 Physics North MC 7300, Berkeley, CA 94720, USA
[3] INAF–Osservatorio Astronomico di Brera, Via Bianchi 46, I-23807, Merate (LC), Itay
[4] Department of Physics & Astronomy, University of Utah, Salt Lake City, UT 84112, USA
[5] Department of Astrophysics/IMAPP, Radboud University, P.O. Box 9010, 6500 GL, Nijmegen, The Netherlands
[6] Department of Physics, Department of Astronomy & Astrophysics, & Center for Multimessenger Astrophysics, Institute for Gravitation & the Cosmos, The Pennsylvania State University, University Park, PA 16802, USA
[7] Yukawa Institute for Theoretical Physics, Kitashirakawa-Oiwake-cho, Sakyo-ku, Kyoto, 606-8502, Japan
[8] Institut de Radioastronomie Millimétrique (IRAM), 300 Rue de la Piscine, 38400 Saint-Martin-d'Hères, France
[9] INAF Istituto di Radioastronomia, via Gobetti 101, 40129 Bologna, Italy
[10] TAPIR, Mailcode 350-17, California Institute of Technology, Pasadena, CA 91125, USA
[11] Research Center for the Early Universe (RESCEU), School of Science, The University of Tokyo, 7-3-1 Hongo, Bunkyo-ku, Tokyo 113-0033, Japan
[12] Department of Astronomy/Steward Observatory, 933 North Cherry Avenue, Rm. N204, Tucson, AZ 85721-0065, USA
[13] National Radio Astronomy Observatory, 520 Edgemont Rd, Charlottesville, VA 22903, USA
[14] SARAO/Hartebeesthoek Radio Observatory, PO Box 443, Krugersdorp 1740, South Africa
[15] Center for Astrophysics | Harvard & Smithsonian, 60 Garden Street, Cambridge, MA 02138-1516, USA
[16] Department of Astronomy, University of Virginia, Charlottesville, VA 22904-4325, USA
[17] Instituto de Ciencias Nucleares, Universidad Nacional Autónoma de México, Apartado Postal 70-264, 04510 México, CDMX, Mexico
[18] Institut d'Astrophysique de Paris, CNRS-Sorbonne Université, 98 bis boulevard Arago, 75014 Paris, France
[19] School of Natural Sciences, Institute for Advanced Study, Princeton, NJ 08540, USA
[20] Space Radiation Laboratory, California Institute of Technology, 1200 E California Blvd Pasadena, CA 91125, USA
[21] Department of Astronomy and Astrophysics, California Institute of Technology, Pasadena, CA 91125, USA
[22] Department of Astronomy, Kyoto University, Kitashirakawa-Oiwake-cho, Sakyo-ku, Kyoto, 606-8502, Japan
[23] Joint Institute for VLBI ERIC, Oude Hoogeveensedijk 4, 7991 PD Dwingeloo, The Netherlands
[24] ASTRON, Netherlands Institute for Radio Astronomy, Oude Hoogeveensedijk 4, 7991 PD Dwingeloo, The Netherlands
[25] Illinois Institute of Technology Department of Physics, Chicago, IL 60616, USA
[26] Purdue University, Department of Physics and Astronomy, 525 Northwestern Ave, West Lafayette, IN 47907, USA
[27] Integrative Data Science Initiative, Purdue University, West Lafayette, IN 47907, USA
[28] Homi Bhabha Centre for Science Education, TIFR, Mumbai 400088, India
[29] Department of Astronomy & Astrophysics, The University of Chicago, Chicago, IL 60637, USA
*Received 2024 November 1; revised 2025 March 5; accepted 2025 March 18; published 2025 May 14*

## Abstract

We present the results from our extensive hard-to-soft X-ray (NuSTAR, Swift-XRT, XMM-Newton, Chandra) and meter-to-millimeter-wave radio (Giant Metrewave Radio Telescope, Very Large Array, NOEMA) monitoring campaign of the very nearby ($d = 6.9$ Mpc) Type II supernova (SN) 2023ixf spanning ≈4–165 days post-explosion. This unprecedented data set enables inferences on the explosion's circumstellar medium (CSM) density and geometry. In particular, we find that the luminous X-ray emission is well modeled by thermal free–free radiation from the forward shock with rapidly decreasing photoelectric absorption with time. The radio spectrum is dominated by synchrotron radiation from the same shock. Similar to the X-rays, the level of free–free absorption affecting the radio spectrum rapidly decreases with time as a consequence of the shock propagation into the dense CSM. While the X-ray and the radio modeling independently support the presence of a dense medium corresponding to an effective mass-loss rate $\dot{M} \approx 10^{-4}\,M_{\odot}\ \mathrm{yr}^{-1}$ at $R = (0.4\text{–}14) \times 10^{15}$ cm (for $v_{\rm w} = 25\ \mathrm{km\ s}^{-1}$), our study points at a complex CSM density structure with asymmetries and clumps. The inferred densities are ≈10–100 times those of typical red supergiants, indicating an extreme mass-loss phase of the progenitor in the ≈200 yr preceding core collapse, which leads to the most X-ray luminous Type II SN and the one with the most delayed emergence of radio emission. These results add to the picture of the complex mass-loss history of massive

* The title was inspired by a news report on the rediscovery of fossilized dinosaur eggs in rural Gujarat in Indian Express 2024 October 28.
[30] Corresponding author.
[31] NASA Hubble Fellow.

stars on the verge of collapse and demonstrate the need for panchromatic campaigns to fully map their intricate environments.

*Unified Astronomy Thesaurus concepts:* Core-collapse supernovae (304); Radio transient sources (2008); X-ray transient sources (1852)

## 1. Introduction

Observations of core-collapse supernovae (CCSNe) across optical, radio, and X-ray wavelengths have provided strong evidence for a time-dependent mass-loss history of massive stars in the centuries preceding core collapse (N. Smith 2014; R. A. Chevalier & C. Fransson 2017). The consequent circumstellar medium (CSM) would be complex, with significant structure in the immediate environments and at farther distances from the explosion site. While the time-dependent mass loss of massive stars is not well understood by the current stellar evolution models, understanding the structure of the CSM could put valuable constraints on various proposed mechanisms of mass loss (e.g., E. Quataert & J. Shiode 2012; E. Quataert et al. 2016; J. Fuller 2017; S. P. Owocki et al. 2017).

Various observational techniques that probe the CSM at different distances from the explosion center include direct detection of preexplosion stellar outbursts (e.g., C. D. Kilpatrick & R. J. Foley 2018; N. L. Strotjohann et al. 2021; W. V. Jacobson-Galán et al. 2022; A. Reguitti et al. 2024); the presence of narrow emission lines in early optical spectra known as "flash spectroscopy" features (e.g., D. C. Leonard et al. 2000; D. Khazov et al. 2016; O. Yaron et al. 2017; I. Boian & J. H. Groh 2020; R. J. Bruch et al. 2021, 2023; G. Terreran et al. 2022; W. V. Jacobson-Galán et al. 2024b, 2024a); or from the properties of early optical light curves (e.g., S. Das & A. Ray 2017; F. Förster et al. 2018). Outside the UV/optical spectrum, the shock interaction with a dense medium manifests as luminous X-ray and radio emission (e.g., R. A. Chevalier & C. Fransson 2017 for a recent review), where X-ray emission typically arises from thermal Bremsstrahlung and radio emission is due to shock-accelerated relativistic electrons producing synchrotron radiation. By analyzing the spectral and temporal evolution of X-ray and radio emission, the CSM density profile can be inferred (e.g., P. Chandra et al. 2012; V. V. Dwarkadas 2014; S. Chakraborti et al. 2016, 2012 for Type II supernovae (SNe)).

SN 2023ixf was discovered by K. Itagaki on 2023 May 19 in the galaxy M101 (NGC 5457). The SN was classified as a Type II based on the optical spectrum (D. A. Perley et al. 2023). We adopt a distance of 6.9 Mpc (A. G. Riess et al. 2022) and a time of first light corresponding to MJD 60082.833 (Y. Mao et al. 2023). All times are reported with respect to the time of first light. The small uncertainty (≈0.02 day) on the time of first light has no impact on our major conclusions.

Extensive data have been collected on SN 2023ixf and its explosion site across the electromagnetic spectrum, including early optical/UV observations sampling the light-curve rise (G. Hosseinzadeh et al. 2023; E. A. Zimmerman et al. 2024), early to late-time optical spectroscopic observations revealing flash ionization features at early times (K. A. Bostroem et al. 2023; D. Hiramatsu et al. 2023; W. V. Jacobson-Galán et al. 2023; N. Smith et al. 2023; R. S. Teja et al. 2023; M. Yamanaka et al. 2023), preexplosion image analysis in optical and IR bands (J. E. Jencson et al. 2023; C. D. Kilpatrick et al. 2023; Z. Niu et al. 2023; J. L. Pledger & M. M. Shara 2023; Y.-J. Qin et al. 2024; M. D. Soraisam et al. 2023; S. D. Van Dyk et al. 2024; D. Xiang et al. 2024; J. M. M. Neustadt et al. 2024; C. L. Ransome et al. 2024), UV spectroscopy (K. A. Bostroem et al. 2024; E. A. Zimmerman et al. 2024), polarimetric observations (S. S. Vasylyev et al. 2023; M. Shrestha et al. 2025; A. Singh et al. 2024), early X-ray (P. Chandra et al. 2023b; B. W. Grefenstette et al. 2023; I. A. Mereminskiy et al. 2023; S. Panjkov et al. 2023) and radio observations (E. Berger et al. 2023; P. Chandra et al. 2023a; D. Matthews et al. 2023b, 2023a).

Here, we present results from our extensive X-ray and radio monitoring campaign of SN 2023ixf spanning $\delta t \approx 4$–165 days. The paper is organized as follows. In Section 2, we present observations and data reduction. Inferences from our multi-epoch broadband X-ray spectral analysis are described in Section 4. In Section 5, we present the modeling of radio synchrotron emission and results. We discuss our findings in Section 6 and conclude in Section 7.

## 2. Observations and Data Reduction

### 2.1. Northern Extended Millimetre Array

We observed the field of SN 2023ixf with the Northern Extended Millimetre Array (NOEMA) under Director's Discretionary Time (project ID d23ab; PI: T. Laskar) in 2023 June and July using the most compact configuration with baselines ranging between 17 m and 175 m. Observations took place over three epochs at 3 mm (tuned to 89.9 GHz in the upper side band) and 2 mm (tuned to 149.9 GHz in the upper side band) each, with ⩽1 day difference per epoch between the two bands. We used dual polarization and an initial spectral resolution of 2 MHz over the full bandwidth. We used the radio star MWC349 for absolute flux calibration for most tracks, except for one track, during which we used the radio star LkHa101. The continuum fluxes of both sources are regularly monitored against planets, giving an uncertainty of about 5%–10% at 3 mm and 10%–15% at 2 mm. The bandpass calibration was done on one of the following sources: 2013+370, 3C273, 1418+546, 3C84, or 2200+420, while the temporal gains on phases and amplitudes were calibrated against 1418+546. Each epoch was observed on-source for about 1.1 hr at 3 mm and between 0.6 hr and 2.1 hr at 2 mm. We calibrated the data with the GILDAS package CLIC, followed by imaging with the Common Astronomy Software Applications (CASA, version 6.5.5.1; J. P. McMullin et al. 2007; CASA Team et al. 2022) using natural weighting. We detect a point source in all three epochs at 3 mm but not at 2 mm. We measured the flux density by fitting a point source at the position of the optical counterpart. We report the details of our observations and flux measurements in Table 6.

### 2.2. Very Large Array

We observed the field of SN 2023ixf with the Karl G. Jansky Very Large Array (VLA) starting from 2023 May 23.01 ($\delta t = 4.2$ days) under project code SF151070 (PI: R. Margutti). Our observations span a time period of $\delta t \approx 4$–165 days, covering frequencies 2–24 GHz with the VLA in A, BnA, and

**Table 1**
Best-fitting Parameters of the Absorbed Thermal Bremsstrahlung Continuum Model for the Five Epochs with Broadband X-Ray Coverage, and for the Last Epoch of CXO Observations

| Time (days) | Instrument | $NH_{int}$[a] ($10^{22}$ cm$^{-2}$) | $T$ (keV) | Log(Flux)[b] 0.3–10 keV | Log(Flux)[b] 0.3–30 keV | Norm[c] ($10^{-4}$) |
|---|---|---|---|---|---|---|
| 4.4 | NuSTAR+XRT | $31.2^{+4.3}_{-7.6}$ | $41.3^{+58.6}_{-9.8}$ | $-11.83^{+0.04}_{-0.08}$ | $-11.47^{+0.04}_{-0.03}$ | $3.55^{+0.20}_{-0.28}$ |
| 11.5 | NuSTAR+XRT+CXO | $3.2^{+0.3}_{-0.3}$ | $61.5^{+22.9}_{-9.4}$ | $-11.77^{+0.01}_{-0.02}$ | $-11.42^{+0.02}_{-0.01}$ | $4.29^{+0.19}_{-0.12}$ |
| 21.4 | NuSTAR+XRT | $1.5^{+0.7}_{-0.3}$ | $31.6^{+6.8}_{-4.8}$ | $-12.08^{+0.02}_{-0.02}$ | $-11.77^{+0.02}_{-0.02}$ | $1.97^{+0.05}_{-0.06}$ |
| 30.5 | NuSTAR+XMM | $0.63^{+0.10}_{-0.12}$ | $31.4^{+13.0}_{-4.4}$ | $-12.23^{+0.01}_{-0.03}$ | $-11.93^{+0.03}_{-0.02}$ | $1.38^{+0.06}_{-0.07}$ |
| 58.4 | NuSTAR+XMM | $0.34^{+0.10}_{-0.09}$ | $22.4^{+10.4}_{-5.8}$ | $-12.52^{+0.02}_{-0.06}$ | $-12.25^{+0.05}_{-0.03}$ | $0.70^{+0.05}_{-0.07}$ |
| 85.7 | CXO | $0.06^{+0.33}_{-0.01}$ | >7 | $-12.58^{+0.06}_{-0.02}$ | $-12.55^{+0.074}_{-0.075}$ | $0.54^{+0.18}_{-0.04}$ |

**Notes.**
[a] Solar abundance assumed.
[b] Unabsorbed, units of erg s$^{-1}$ cm$^{-2}$.
[c] The normalization of the Bremsstrahlung model is defined as Norm $\equiv \frac{3.02\times10^{-15}}{4\pi d^2}\int n_e n_I dV$, where $n_e$/cm$^{-3}$ and $n_I$/cm$^{-3}$ are the electron and ion number densities, respectively, and $d$ cm$^{-1}$ is the distance to the target.

D configurations. We used 3C286 as the flux density and bandpass calibrator and J1419+5423 as the phase calibrator. The data were calibrated using the VLA calibration pipeline in CASA version 6.4.1.12 and imaged using task TCLEAN (A. R. Offringa & O. Smirnov 2017) adopting natural weighting. We performed phase-only self-calibration where necessary.

Radio emission was not detected in our observation on 2023 May 23.01 ($\delta t = 4.2$ days) with a $5\sigma$ flux density limit of $F_\nu < 33\ \mu$Jy (D. Matthews et al. 2023b). We detected radio emission from the SN on 2023 June 17.04 ($\delta t = 29.2$ days) with a flux density of $F_\nu = (41 \pm 8)\ \mu$Jy at 10 GHz (D. Matthews et al. 2023a). The flux density and position of the emission were measured using task IMFIT that fits an elliptical Gaussian of the size of the synthesized beam at the source position in the image plane. The SN was detected at multiple frequencies in the successive epochs of observations. We present the flux densities in Table 6 and spectra in Figure 1. The VLA was in D configuration on 2023 October 31 ($\delta t \approx 165$ days), and the SN emission was unresolved with other nearby sources in the 2–5 GHz maps, resulting in relatively high flux density limits.

### 2.3. Giant Metrewave Radio Telescope

We observed the field of SN 2023ixf with the Giant Metrewave Radio Telescope (GMRT) from 2023 May 21 ($\delta t \approx 2$ days) to 2023 October 31 ($\delta t \approx 165$ days) under project codes 44_095 and 45_091 (PI: Poonam Chandra). The data were recorded in standard continuum mode in bands 4 (550–850 MHz) and 5 (1050–1450 MHz) with a bandwidth of 400 MHz split into 2048 channels. 3C286 was used as the flux density and bandpass calibrator, whereas J1400+621 was used as the phase calibrator. We processed the raw visibilities using Astronomical Image Processing Software (AIPS; E. W. Greisen 2003) following standard procedure (A. J. Nayana et al. 2017). The data were initially flagged and calibrated using various AIPS tasks. The fully calibrated target source data were imaged using task IMAGR. We performed a few rounds of phase-only self-calibration to improve the image fidelity.

Radio emission was not detected until 2023 October 30 ($\delta t \approx 165$ days), resulting in a $3\sigma$ flux density upper limit

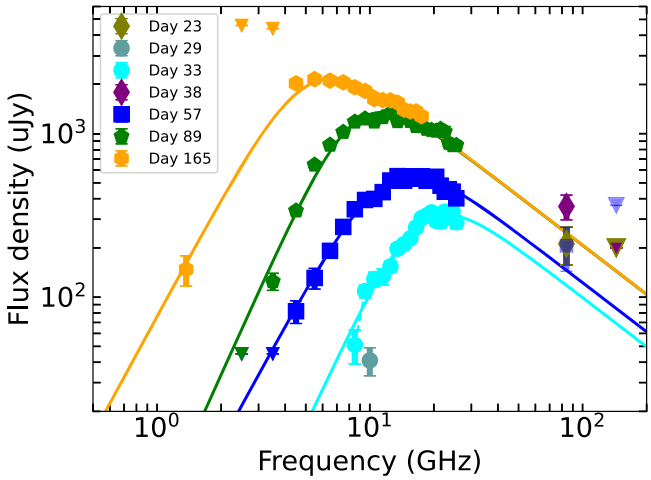


**Figure 1.** Radio spectra of SN 2023ixf in the time range $\delta t = 23$–165 days. The flux density measurements at 84 GHz obtained using NOEMA are marked as diamonds. Inverted triangles mark the $5\sigma$ flux density upper limits. Solid lines represent best-fit BPL models with a smoothing parameter fixed to $s = -1$ and an optically thin spectral index fixed to $\alpha_1 = -1$.

$F_\nu < 75\ \mu$Jy at 1.25 GHz (P. Chandra et al. 2023a) and $F_\nu < 90\ \mu$Jy at 0.65 GHz. We detected radio emission from the SN with a flux density $F_\nu = (148 \pm 31)\ \mu$Jy at 1.25 GHz on 2023 October 30 ($\delta t \approx 165$ days). The flux density was measured by fitting an elliptical Gaussian at the SN position in the image plane using task JMFIT. Details of GMRT observations and flux measurements are reported in Table 8.

### 2.4. Swift X-Ray Telescope

The X-Ray Telescope (XRT; D. N. Burrows et al. 2005) onboard the Neil Gehrels Swift Observatory (N. Gehrels et al. 2004) started observing SN 2023ixf on 2023 March 20 UT06:25:01 ($\delta t \approx 1.4$ days). Here we present the analysis of XRT observations acquired until 2023 October 18. Data have been processed with HEASoft v6.33 and corresponding calibration files. We extracted a 0.3–10 keV count-rate light curve and rebinned to minimum count rate following standard procedures (P. A. Evans et al. 2009; R. Margutti et al. 2013). We extracted 12 post-explosion spectra at salient phases of the SN X-ray light curve and around the time of acquisition of

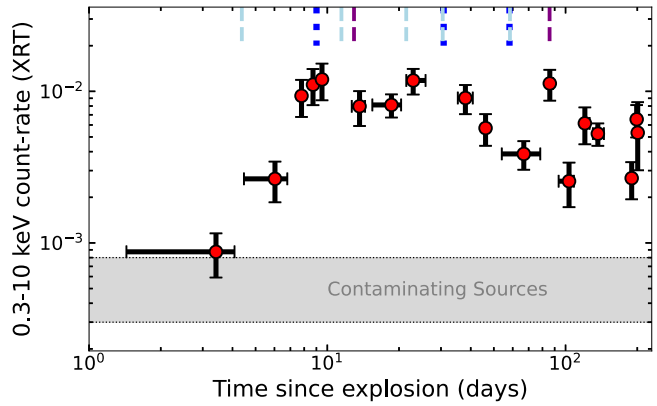


**Figure 2.** Post-explosion Swift-XRT count-rate light curve. Vertical lines mark the time of XMM-Newton (dark blue, dotted), NuSTAR (light blue, dashed), and CXO (purple, dashed) observations (some epochs are coordinated). The gray area marks the range of the preexplosion X-ray emission due to contaminating sources as detected by Swift-XRT. The observed steep count-rate increase at early times mostly results from the rapidly decreasing intrinsic hydrogen column density with time accompanied by cooling (Figure 7).

NuSTAR observations (Table 1). The Swift-XRT and the broadband (soft and hard X-rays) spectral fitting are described in Section 3.

Swift-XRT serendipitously observed the location of SN 2023ixf on a number of occasions starting ≈6700 days before the explosion. X-ray emission is detected at the location of SN 2023ixf at the level of $\approx 4 \times 10^{-4}$ c s$^{-1}$ (0.3–10 keV), which corresponds to a flux in the range $\approx(5\text{–}10) \times 10^{-15}$ erg s$^{-1}$ cm$^{-2}$ in the very soft energy band 0.3–1 keV for an assumed power-law model with a photon index in the range $\Gamma = 2\text{–}4$. This emission is physically unrelated to SN 2023ixf. The X-ray spectrum at very soft energies (<1 keV) at early times ($\delta t < 10$ days) when the SN 2023ixf emission is heavily absorbed is the most affected by the contaminating emission. XMM-Newton and CXO observations (Sections 2.5–2.6) reveal that this "host-galaxy background" flux mostly results from the presence of three X-ray sources within ≈40″ of SN 2023ixf that contaminate the Swift-XRT point-spread function (PSF). Consistent with the conclusion of S. Panjkov et al. (2023), we ascribe the observed time variability of the X-ray emission in preexplosion images to the contamination by physically unrelated nearby sources.

X-ray emission at the location of SN 2023ixf is detected starting at around ≈4 days, and we show the Swift-XRT count-rate light curve of SN 2023ixf in Figure 2. Accurate time-dependent flux calibration is performed as described in Section 3. We note that we quantitatively accounted for the contaminating flux using the spectral model derived from preexplosion XMM-Newton observations in Section 2.6.

### 2.5. Chandra X-Ray Observatory

The X-Ray Telescope (CXO) started observing SN 2023ixf on 2023 March 31 (obs ID 27862, $\delta t = 12.84$ days) for an exposure time of 20.1 ks, with a second epoch of CXO observations acquired starting on 2023 August 11 ($\delta t \approx 85$ days, obsIDs 27863 and 28374 for a total exposure of 20.9 ks, P. Chandra). CXO ACIS-S data have been reduced following standard practice within `CIAO v4.15` and corresponding calibration files. A bright X-ray source is detected with high confidence at the location of SN 2023ixf (Table 9). The detection significance was estimated with `wavdetect`. We extracted a spectrum with `specextract` using a source region with a radius of 2″ (first epoch) and 1.″5 (second epoch). The background was estimated from a source-free region with a radius of 33.″5. While extensive CXO preexplosion observations at the SN 2023ixf location exist (and no evidence for X-ray emission has been found; B. W. Grefenstette et al. 2023), the sharp PSF of the CXO implies that contamination by unrelated sources is not an issue for CXO observations of SN 2023ixf. Spectral modeling is described in Section 3.

### 2.6. XMM-Newton

A sequence of three deep XMM-Newton observations of SN 2023ixf have been acquired in the time range $\delta t \approx 9.0\text{–}58.2$ days (PIs Campana, Margutti). Details are reported in Table 9. We reduced and analyzed the data of the three European Photon Imaging Cameras (EPIC)-pn, MOS1, and MOS2 using the Scientific Analysis System v.20.0.0 and corresponding calibration files (CALDB 3.13). We filtered out the intervals of time affected by severe proton flaring with the `espfilt`[32] task, which led to a significant reduction of the effective exposure time of the third XMM-Newton observation (Table 9). A bright X-ray source is detected in all observations at the location of SN 2023ixf, with count rates reported in Table 9. To assess the significance of the detection, we ran the task `edetect_chain`. For each of the three XMM-Newton epochs, we extracted three source spectra (i.e., one for the EPIC-pn, MOS1, and MOS2) using a region with a 20″ radius to minimize the impact of the contamination by nearby X-ray sources (Figure 3).

To further quantitatively assess the level of contamination of post-explosion XMM-Newton observations of SN 2023ixf by physically unrelated sources, we used a deep XMM-Newton preexplosion observation of the SN field acquired in 2018 (Obs ID 0824450501, PI G. Israel; effective exposure time after accounting for proton flaring of 55.5 ks). Significant X-ray emission with a very soft spectrum is detected at energies $\lesssim$5 keV in a 20″ region centered at the SN location. The EPIC-pn spectrum is well fit by a simple-power-law model (`tbabs*pow`, phenomenological model) with best-fitting photon index $\Gamma = 5.5^{+1.0}_{-0.6}$ and hydrogen absorption column density $\mathrm{NH_{pre}} = (0.44^{+0.14}_{-0.11}) \times 10^{22}$ cm$^{-2}$. The corresponding observed flux in the 0.3–1 keV energy range is $F_{\mathrm{X,pre}} = (6.4^{+0.4}_{-0.6}) \times 10^{-15}$ erg s$^{-1}$cm$^{-2}$. This flux estimate is consistent with our inferences based on preexplosion Swift-XRT observations (Section 2.4). It follows that the contamination by nearby sources can have a nonnegligible effect either (i) at early times $\delta t < 9$ days when the X-ray emission of SN 2023ixf is highly absorbed, and the contaminating flux can dominate the observed emission in the very soft (e.g., 0.3–1 keV) energy range; or (ii) at very late times when the SN 2023ixf emission becomes faint and eventually comparable to the astrophysical background.

Case (i) applies to the first XMM-Newton epoch and to early Swift-XRT observations acquired at $\delta t \lesssim 12$ days (i.e., during the rise time of the observed light curve). We show in Figure 4 (left panel) the first XMM-Newton spectrum where the presence of an excess of very soft X-ray emission at energies $\lesssim$1 keV compared to the absorbed thermal Bremsstrahlung model is apparent. Modeling the excess of emission with an absorbed power-law model leads to parameter inferences that

[32] https://xmm-tools.cosmos.esa.int/external/sas/current/doc/espfilt/espfilt.html

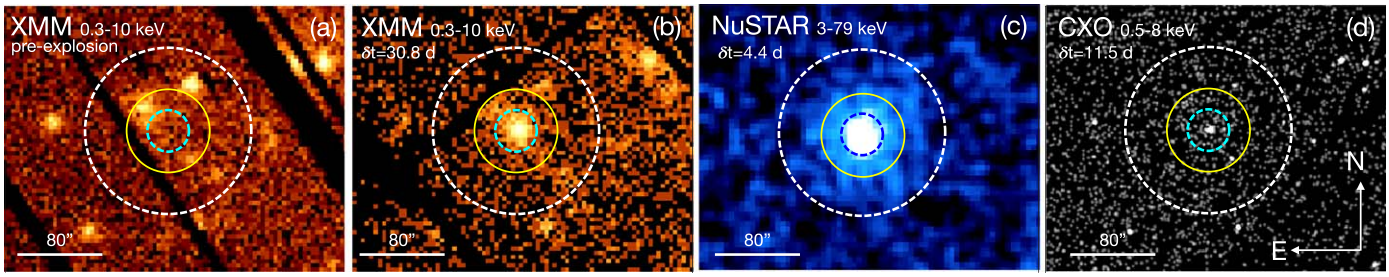


**Figure 3.** Preexplosion (panel (a), obs ID 0824450501, exposure of ∼55 ks) and post-explosion (panel (b), obs ID 0921180101, exposure of 10 ks) XMM-Newton/EPIC-pn soft X-ray images of the field of SN 2023ixf, showing the presence of three unrelated sources within 40″ (yellow region) that contaminate the XMM-Newton and Swift-XRT PSF. Panel (c): NuSTAR hard X-ray image of the field (obs ID 90902520002, exposure of ∼42 ks). Panel (d): Thanks to the significantly sharper PSF, contamination by unrelated sources is not an issue for CXO observations of SN 2023ixf (obs ID 27862, exposure of ∼20 ks). Dashed cyan or blue region: 20″ radius region at the location of SN 2023ixf. Yellow region: 40″ radius region (which is representative of the XMM-Newton and XRT PSF). The dashed white region has a radius of 80″.

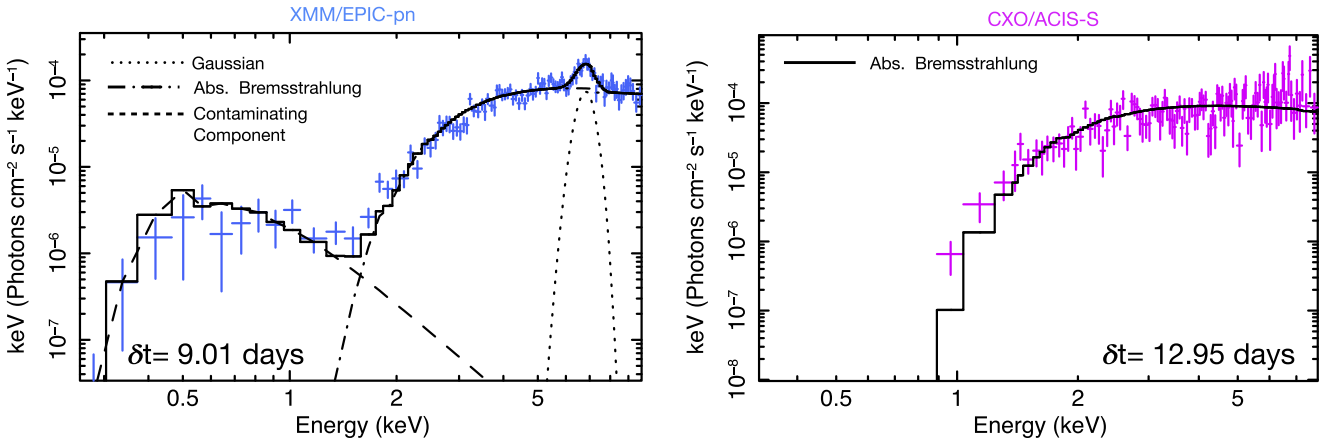


**Figure 4.** Left panel: XMM-Newton EPIC-pn unfolded $F_\nu$ spectrum at $\delta t = 9.01$ days showing a clear evidence for an excess of soft X-ray emission at <1 keV with respect to an absorbed thermal Bremsstrahlung model. A Gaussian profile has been added to model the Fe line emission at ≈6.8 keV. Right Panel: CXO ACIS-S unfolded spectrum of SN 2023ixf at $\delta t = 12.95$ days with best-fitting absorbed thermal Bremsstrahlung model. Since (i) the soft X-ray component in the XMM-Newton spectrum has properties consistent with those inferred from preexplosion observations; and (ii) CXO observations with significantly sharper PSF do not require the addition of a soft X-ray component, we conclude that there is no compelling observational evidence that the soft X-ray excess of emission is physically related to SN 2023ixf and we thus ascribe that to contamination by unrelated sources in the host galaxy (Figure 3).

are statistically consistent with those derived from the preexplosion spectrum (with a 0.3–1 keV flux of $F_X \approx 2 \times 10^{-15}$ erg s$^{-1}$ cm$^{-2}$, even lower than in preexplosion images). CXO observations acquired ≈4 days later do not provide evidence for the presence of a soft X-ray excess. Taken at face value, the excess of soft X-ray emission can also be explained by a partial covering fraction of the absorber. However, given the consistency of the soft X-ray component detected by XMM-Newton with preexisting emission at the location of SN 2023ixf, and the lack of evidence for this component in CXO data, in the following we proceed under the hypothesis that the soft X-ray excess of emission is physically unrelated to SN 2023ixf and more likely associated with emission of nearby X-ray sources that contaminate the wider XMM-Newton and Swift-XRT PSF. CXO and NuSTAR observations are unaffected because of the significantly sharper PSF (CXO) and the harder energy response (NuSTAR).

### 2.7. NuSTAR (3–79 keV)

B. W. Grefenstette et al. (2023) presented the analysis of the first two epochs of NuSTAR data. Here we present the homogeneous analysis of the entire NuSTAR data set of SN 2023ixf, which comprises five epochs of observations acquired between $\delta t \approx$ 4.3–58.4 days (PIs Grefenstette, Margutti). Details are provided in Table 9. We extracted spectra and response files using the NuSTAR Data Analysis Software (v2.1.2) and calibration files (version 20240104) with `nupipeline` and `nuproducts`. For the source, we used an extraction region with a radius varying from 80″ (at maximum source brightness) to 50″ (at minimum source brightness) to maximize the signal-to-noise ratio. A nearby source-free region was used to estimate the local background. We checked for the presence of solar flares and significant radiation belt backgrounds using the standard background plots. We did not find any, so we used the standard nustardas filtering. In the following, we thus proceed with data products from the standard `nupipeline` extraction, which benefits from the larger number of counts. Spectral modeling is done jointly with the soft X-ray data in Section 3.

## 3. Joint Soft and Hard X-Ray Spectral Modeling and X-Ray Flux Calibration

Broad-band X-ray spectral modeling is necessary to reliably estimate the spectral parameters and to constrain the physical properties of the emitting region. Below, we first perform joint soft and hard X-ray spectral modeling for the five epochs in the time range $\delta t =$ 4.4–58.4 days for which SN 2023ixf was observed with NuSTAR in coordination with soft X-ray telescopes (Swift-XRT, XMM-Newton, or CXO) (Figure 5). We then use the spectral parameters from this broadband

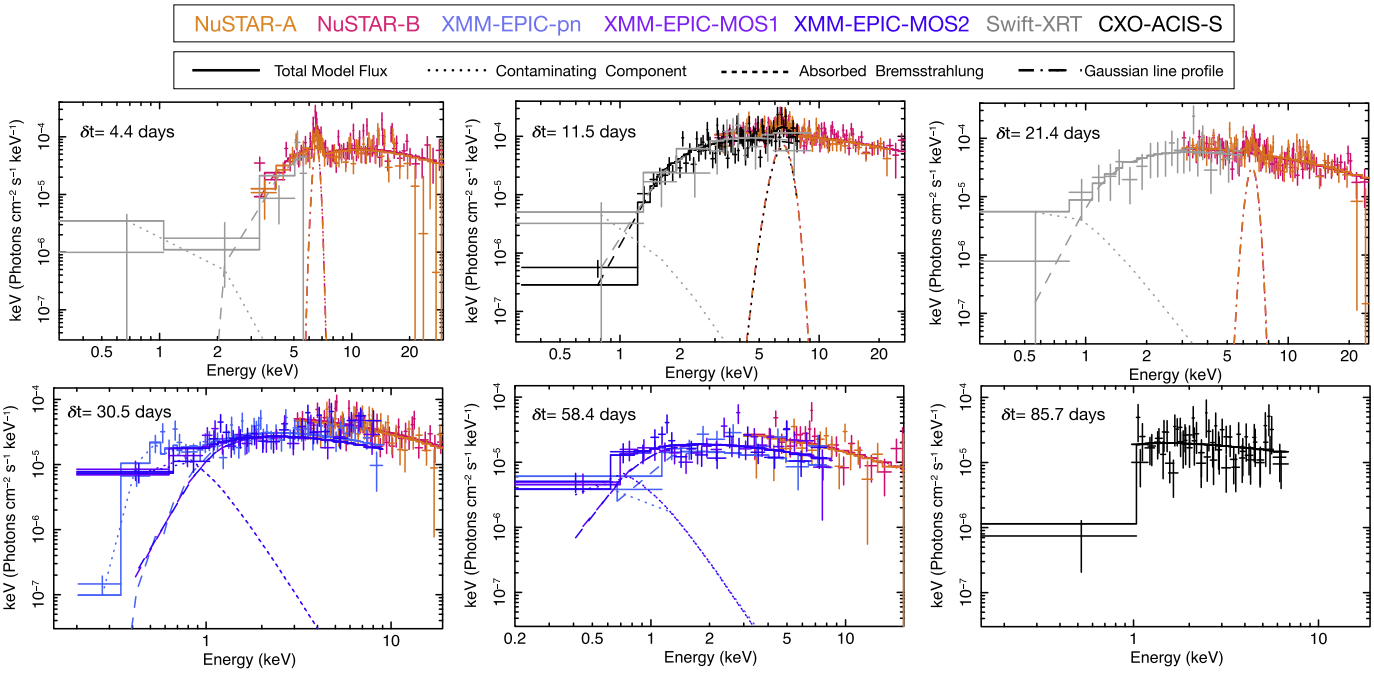


**Figure 5.** Unfolded $F_\nu$ broadband X-ray spectra for the six epochs for which we report the best-fitting parameters in Table 1. In all cases the data are best fit by an absorbed thermal Bremsstrahlung model (long dashed lines) with a decreasing level of intrinsic absorption with time. Dotted lines: contamination component from unrelated sources in the host galaxy. Fe emission, here modeled with a Gaussian profile (dotted–dashed line), is clearly detected in the first three epochs. Data have been rebinned for displaying purposes only. CXO data below 0.5 keV are here shown for comparison but have not been used for fitting.

analysis to anchor the flux calibration of the intermediate epochs when only soft X-ray data are available.

As observationally confirmed by the extensive campaign of SN 2014C (R. Margutti et al. 2017; D. Brethauer et al. 2022; B. P. Thomas et al. 2022), the X-ray emission from SN shocks that interact with dense material is expected to be (i) highly absorbed, (ii) with a level of absorption that decreases with time, and (iii) of thermal nature. SN 2023ixf broadly confirms these expectations and also shows an excess of emission around ∼6.5 keV that has been attributed to Fe K$\alpha$ lines in strongly interacting SNe such as 2014C. We use a Galactic neutral hydrogen (NH) column density in the direction of SN 2023ixf of $\mathrm{NH_{MW}} = 7.9 \times 10^{20}\,\mathrm{cm^{-2}}$ (HI4PI Collaboration et al. 2016).[33] We adopt the solar abundances as updated in M. Asplund et al. (2009; i.e., `abund aspl` within `Xspec`[34]). We first use `apec` to simulate the spectrum of a collisionally ionized plasma (continuum and corresponding line emission). However, a single-temperature component `apec` model fails to simultaneously reproduce the bright Fe line emission and the underlying continuum, as expected. We comment on the implications of this finding in Section 4. The maximum temperature $T = 64$ keV allowed within the `apec` model is also not physical for this case. We thus proceed with an absorbed thermal Bremsstrahlung model (`tbabs*ztbabs*bremss` within `Xspec`) for the continuum, and we model the excess of emission with a Gaussian line profile. For XMM-Newton (EPIC-pn, MOS1, and MOS2) and Swift-XRT observations, we model the contamination by nearby X-ray sources adopting as a phenomenological model an absorbed power law (`tbabs*pow`) with photon index and neutral hydrogen column densities frozen to the best-fitting values obtained from deep preexplosion XMM-Newton observations (Section 2.6) and normalization free to vary to account for potential time variability of the emission from the contaminating sources when needed (as observed by Swift-XRT, Section 2.4; see also S. Panjkov et al. 2023). Finally, we account for uncertainties affecting the instrumental cross calibration in the absolute flux phase space by adding a multiplicative factor to the model. Absolute fluxes are reported with respect to NuSTAR module A. We employ the W statistic and we self-consistently derive the parameter uncertainties with Markov Chain Monte Carlo (MCMC). The best-fitting model parameters are listed in Tables 1 and 2 for the Bremsstrahlung continuum and the emission line profile, respectively.

We model the Swift-XRT, XMM-Newton, and CXO spectra without a NuSTAR counterpart using an absorbed Bremsstrahlung spectrum with temperature and neutral hydrogen absorption fixed at the values obtained by interpolating those derived from the joint spectral analysis above. The results from this analysis are then used to derive a time-dependent count-to-

**Table 2**
Best-fitting Parameters of the Fe Emission Modeled with a Gaussian Profile Centered at $E_0$ with Standard Deviation $\sigma$

| Time (days) | $E_0$ (keV) | $\sigma$ (keV) | Log(Flux)[a] |
|---|---|---|---|
| 4.4 | $6.54^{+0.06}_{-0.08}$ | 0.2[b] | $-13.06^{+0.07}_{-0.10}$ |
| 11.5 | $6.52^{+0.07}_{-0.11}$ | $0.58^{+0.20}_{-0.07}$ | $-12.77^{+0.09}_{-0.03}$ |
| 21.4 | $6.61^{+0.14}_{-0.12}$ | $0.33^{+0.22}_{-0.11}$ | $-13.39^{+0.11}_{-0.19}$ |

**Notes.**
[a] Unabsorbed, 0.3–10 keV, units of erg $\mathrm{s^{-1}\,cm^{-2}}$.
[b] Set by the instrumental resolution.

[33] Adopting the lower value of $\approx 2 \times 10^{20}\,\mathrm{cm^{-2}}$ inferred by R. Willingale et al. (2013) based on the X-ray afterglow of gamma-ray bursts has no impact on our major conclusions.
[34] We note that using the default solar abundances in `Xspec` (i.e., those from E. Anders & N. Grevesse 1989) results in NH estimates that are a factor ∼2 different.

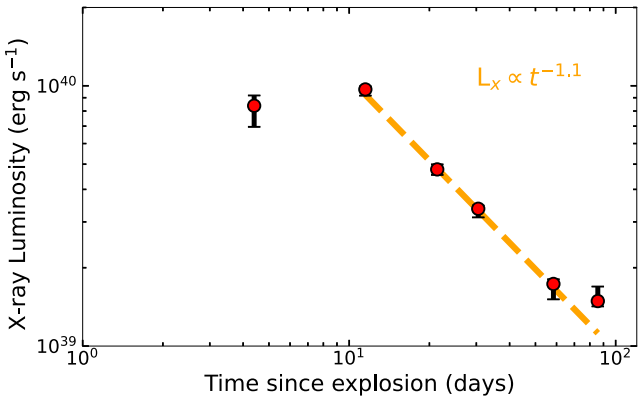


**Figure 6.** Unabsorbed 0.3–10 keV X-ray luminosity of SN 2023ixf (red points) estimated using the broadband X-ray spectral modeling of Section 3 that properly accounts for the spectral evolution of the source with time. We find that $L_X$ is roughly constant at $\delta t \lesssim 10$ days (i.e., before the emergence of broad UV spectral features, E. A. Zimmerman et al. 2024) and later decays as $L_X \propto t^{-1.1}$ (orange dashed line).

flux (absorbed and unabsorbed) conversion factor. Our 0.3–10 keV and 0.3–30 keV flux-calibrated light-curve data are reported in Table 1. The last epoch of CXO observations acquired at $\delta t = 85.7$ days constraints the plasma temperature to values $T > 7$ keV, and it is consistent with minimal intrinsic absorption $NH_{int} \approx 0.06 \times 10^{22}$ cm$^{-2}$ (albeit we note that the upper bound of this parameter is poorly constrained).

We end with a comparison with results from the analysis of partial X-ray data sets of SN 2023ixf that have appeared in the literature. First, by performing a time-resolved soft and hard X-ray joint spectral fitting, we do not confirm the findings of a two-temperature continuum by S. Panjkov et al. (2023). We ascribe the difference to their method of fitting a time-averaged spectrum of a source that is strongly temporally evolving both in terms of absorption column and temperature of emission (while also not accounting for the soft contamination component from the host galaxy). Second, while the observed (i.e., absorbed) 0.3–10 keV flux (or count-rate) light curve of SN 2023ixf shows a marked rise with time until $\delta t \approx 10$ days to then "plateau" until $\delta t \approx 200$ days (Figure 2), we find that this apparent behavior is due to the combined evolution of $T(t)$ and $NH_{int}(t)$ to lower values and does not represent the intrinsic evolution of the X-ray luminosity from SN 2023ixf. Differently from S. Panjkov et al. (2023) and E. A. Zimmerman et al. (2024), our time-resolved broadband X-ray spectral analysis indicates that the intrinsic broadband 0.3–10 keV luminosity of SN 2023ixf is $L_X \approx 10^{40}$ erg s$^{-1}$ for $\delta t \approx 4$–10 days and shows a clear evidence for a temporal decay as $L_X \propto t^{-1.1}$ at $\delta t \gtrsim 10$ days (Figure 6). While based on more extensive broadband X-ray observations, our X-ray modeling is overall consistent with P. Chandra et al. (2023b). Finally, we confirm the evolution toward larger values of the Fe line width with time, as was reported by B. W. Grefenstette et al. (2023), which most likely results from the emergence of Fe emission with different stages of ionization (i.e., from mostly neutral to higher levels of ionization).

## 4. Inferences from X-Ray Observations

The broadband X-ray spectrum of SN 2023ixf observed starting from day ≈4 is of thermal origin, and there is no evidence for a dominant nonthermal component at any time. The observed soft X-ray flux (or count-rate) rises as a consequence of the decreasing absorption with time, which results from the shock expansion through the medium and, possibly, from the larger ionization of the CSM with time. The intrinsic $L_X$ remains roughly constant until $\delta t \approx 10$ days and later decays[35] as $L_X \propto t^{-1.1}$.

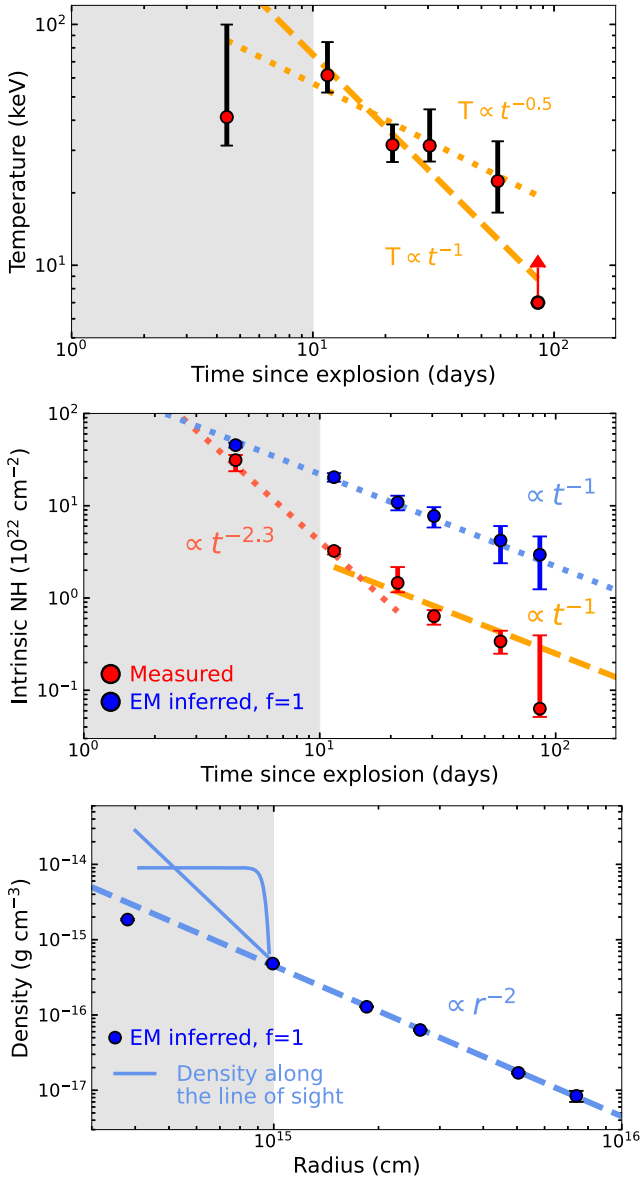


**Figure 7.** Evolution of the X-ray-emitting electron temperature (upper panel), intrinsic neutral hydrogen column density (middle panel), and density (lower panel) as inferred from the modeling of the broadband observations (Section 3). The dashed and dotted lines have been added to guide the eye. For comparison, $NH_{int} \propto t^{-1}$ is expected for a shock evolution in a wind-density profile $\rho_{CSM} \propto r^{-2}$ with constant neutral fraction and an emitting radius $R_{sh} \propto t$. The absorption column of a radiatively cooling shell in the RS would also evolve $\propto t^{-1}$ for a constant mass-loss rate scenario (e.g., T. K. Nymark et al. 2006). The gray area at $\delta t < 10$ days (or $r < 10^{15}$ cm) highlights the period of strong interaction (i.e., narrow lines present in the optical spectra). The EM-inferred $NH_{int}$ and density (blue filled circles) assume a filling factor $f = 1$. The blue solid lines in the lower panel show two examples of density profiles along our line of sight that satisfy the observational constraints of Section 4.

The shock velocity determines the energy imparted to particles crossing it. It follows that the post-shock plasma

[35] The actual index depends on the X-ray energy band considered. Here, we quote the value for 0.3–10 keV.

temperatures for the forward shock (FS) and the reverse shock (RS) are expected to be different, giving an indication of which shock is dominating the emission. The large electron temperatures $k_b T_e \geqslant 50$ keV ($T_e > 6 \times 10^8$ K) inferred in the first epoch at ≈10 days (Table 1, Figure 7) implies that the emitting region is the forward-shocked CSM. The ion temperature of the shocked CSM gas is:

$$T_{i,\rm FS} \approx 1.36 \times 10^9 \left(\frac{n-3}{n-s}\right)^2 \left(\frac{v_{\rm sh}}{10^4\ {\rm km\ s^{-1}}}\right)^2 K \quad (1)$$

(e.g., C. Fransson et al. 1996, their Equation (3.1), where $n$ parameterizes the outer ejecta density profile $\rho_{\rm ej}(r) \propto r^{-n}$, the CSM density scales as $\rho_{\rm CSM} \propto r^{-s}$, and we have assumed solar abundances. For $n = 12$, as appropriate for the convective envelope of a red supergiant (RSG) star (C. D. Matzner & C. F. McKee 1999; S. Ro & C. D. Matzner 2013), and a wind-density profile (Section 4.1), $k_b T_{i,\rm FS} \approx 100$ keV. For the same choice of parameters, shock jump conditions predict a reverse shock temperature that is a factor ≈80 lower:

$$T_{i,\rm RS} = \frac{T_{i,\rm FS}}{(n-3)^2}, \quad (2)$$

which implies $T_{i,\rm RS} \sim 0.5$ keV. This value is consistent with shock temperatures found in other nonstrongly interacting Type IIP SNe (e.g., SNe 2004dj and 2013ej, S. Chakraborti et al. 2012, 2016; Section 6.1) but significantly lower than in SN 2023ixf. Furthermore, in general $T_e \leqslant T_i$ (e.g., C. Fransson et al. 1996, their Figure 5), and in the absence of electron–ion equipartition $T_e \ll T_i$ (Section 4.3). We thus model the detected X-ray emission from SN 2023ixf in the context of an FS origin, and we demonstrate below that this scenario is self-consistent.

### 4.1. CSM Density Profile and Geometry

The broadband X-ray observations of SN 2023ixf provide two complementary ways to estimate the CSM density profile $\rho_{\rm CSM}(r)$: first, the normalization of the Bremsstrahlung spectrum is directly proportional to the emission measure (EM) EM $\equiv \int n_e n_I dV$, where $n_e$ and $n_I$ are the electron and ion number densities in the emitting volume $V$; second, the measured $\rm NH_{int}$ provides an estimate of the material along the line of sight (Table 1). The first method is sensitive to ionized material that is responsible for the detected emission, while the second method is sensitive to the column density of neutral material ahead of the shock[36] and along our line of sight (and does not "know" of the three-dimensional geometry of the CSM surrounding the explosion).

We follow the formalism of D. Brethauer et al. (2022), where a similar model was developed for the strongly interacting SN 2014C. The unshocked CSM density is:

$$\rho_{\rm CSM}(r) = \frac{m_p}{4}\left(\frac{2 \times {\rm EM}(r)\mu_e\mu_I}{V_{\rm FS}(r)}\right)^{1/2}, \quad (3)$$

Where $\mu_e$ and $\mu_I$ are the mean molecular weight per electron and per ion, respectively; $m_p$ is the proton mass; we have assumed a strong shock (for which shock jump conditions dictate a compression factor $\Re = 4$ for gas with adiabatic index $\gamma_{\rm ad} = \frac{5}{3}$), and we accounted for the fact that only half of the emitted radiation reaches the observer (following C. Fransson et al. 1996). We parameterize the emitting volume as a portion of a shell of inner radius $R_{\rm in}$ and outer radius $R_{\rm out}$, with $R_{\rm out} \approx 1.2 R_{\rm in}$ and filling factor $f$: $V_{\rm FS} = \frac{4\pi}{3} f (R_{\rm out}^3 - R_{\rm in}^3)$. The 1.2 factor is motivated by the self-similar solutions for the FS region for a wind-like CSM (see below) and a stellar progenitor with $\rho_{\rm ej}(r) \propto r^{-n}$ and $n \geqslant 9$ (for RSGs $n \approx 12$), R. A. Chevalier (1982). It follows that $\rho_{\rm CSM} \propto f^{-1/2}$. We further assume solar composition for the CSM (i.e., $\mu_e = 1.14$ and $\mu_I = 1.24$; E. A. Zimmerman et al. 2024 infer a metallicity $Z = 0.95\, Z_\odot$ for the environment of SN 2023ixf) and an average FS shock velocity $v_{\rm sh} \approx 10^4\ {\rm km\ s^{-1}}$. Accounting for the mild shock deceleration during the first ≈100 days ($v_{\rm sh} \propto t^{-0.1}$ for the self-similar solutions of R. A. Chevalier (1982) for $n = 12$ and a wind-like CSM) has no impact on the major conclusions from this study.

The CSM density profile inferred from the emission properties of the Bremsstrahlung spectrum is displayed in Figure 7, lower panel, for filling factor $f = 1$, and shows a remarkable agreement with a wind-like density profile $\rho_{\rm CSM} \propto r^{-2}$ at $r \geqslant 10^{15}$ cm. At $r < 10^{15}$ cm, there is a clear deviation from a wind-density profile. This behavior is mirrored by the measured $\rm NH_{int}(t)$: while at late times ($\delta t > 10$ days), $\rm NH_{int}(t)$ displays the $\rm NH_{int}(t) \propto t^{-1}$ evolution that is expected for a wind-density profile, the very early evolution is significantly steeper ($\rm NH_{int}(t) \propto t^{-2.3}$), and suggests a deviation from a wind-density profile with constant level of ionization along the line of sight.

There are three main ways to reconcile the apparent discrepancy between the temporal evolution of the total H column density calculated from Equation (3) and the measured $\rm NH_{int}(t)$ at $\delta t < 10$ days: (i) a time-evolving ionization fraction of the CSM ahead of the FS shock, as a consequence of the ionizing power of the FS radiation; (ii) global CSM asymmetries; (iii) presence of CSM clumps in the innermost CSM $r < 10^{15}$ cm along the line of sight. Each of these three factors is likely to play some role in SN 2023ixf. Below, we try to isolate the main factor that shapes the observed phenomenology.

A comparison between the measured and EM-inferred $\rm NH_{int}$ of Figure 7 would lead to the conclusion that the neutral column fraction evolves from ≈70% at 4 days to ≈15% at later epochs. While the emergence of a line complex around 6.5 keV suggests an increasing level of ionization with time (Section 4.2), we find it unlikely that the drastic change of neutral column fraction between 4 and 10 days is only the result of photoionization by the FS expanding in a wind-density medium (see, e.g., the numerical simulations by C. Fransson et al. 1996). A more likely scenario is one where we are underestimating the density along the line of sight. This can either result from a global asymmetry of the CSM (i.e., $f < 1$) and/or from clumps of material along the line of sight that affect the $\rm NH_{int}$ measure but leave the EM mostly unaffected. The rapid evolution of the optical spectropolarimetric properties of SN 2023ixf at early times (S. S. Vasylyev et al. 2023) points at clear deviations from spherical symmetry, while the detection of Fe emission in the X-ray spectra indicates the presence of higher-density regions (of a factor ≈25 compared to the X-ray continuum producing medium, Section 4.2). Figure 7 (lower panel, solid lines) shows two examples of

[36] The shape of the absorbed continuum of Figure 5 at ⩽a few keV is consistent with being dominated by a neutral absorber.

density profiles along the line of sight that would lead to a constant neutral hydrogen column fraction of ≈15% at all radii, including at $r < 10^{15}$ cm. If attributed to a global CSM asymmetry, the implied filling factors would be unphysically large $f \approx 25$–400. Instead, density clumps are more likely, and we note that the overdensity of a factor ≈20 at small radii along the line of sight is intriguingly similar to the inferred density of the Fe-line-emitting material.

Finally, the constraints on the column density of ionized CSM material imply an electron scattering optical depth $\tau_{es} \leqslant 0.2$ at $\delta t \geqslant 4$ days for the "average" medium and $\tau_{es} \leqslant 1$ at $\delta t \geqslant 4$ days for medium along the line of sight. The detection of emission lines with prominent Lorentzian wings in the optical/UV requires instead significantly larger $\tau_{es} >$ a few at $\delta t \lesssim 10$ days (e.g., W. V. Jacobson-Galán et al. 2023), from which we conclude that the region of optical/UV line formation is distinct from the X-ray emitting region even when the two types of emission coexist in time. This finding translates into density estimates that differ by a factor of ≈10–100 at the same radii $r \leqslant 10^{15}$ cm, with the optical/UV emission originating from the densest regions (discussed in Section 6.2). Parenthetically, the low $\tau_{es}$ implies that Comptonization of the most energetic X-ray photons has no dominant effect in the X-ray emitting regions.

To conclude this section, our modeling of the X-ray emission from SN 2023ixf thus suggests an anisotropic and/or clumpy X-ray emitting CSM. The overall density profile is not too dissimilar from a wind at $10^{15} < r < 10^{16}$ cm. However, the innermost CSM region at $r < 10^{15}$ cm is considerably more complex, with overdensities and deviations from spherical symmetry.

### 4.2. Inferences from the Fe Kα Line

At the measured $T_e \approx 5 \times 10^8$ K free–free cooling dominates (e.g., C. Fransson et al. 1996), and no prominent emission line is expected. However, the X-ray spectra of Figure 5 show a prominent feature around 6–7 keV that we interpret as Fe Kα emission. For line emission to be prominent, gas temperatures $T \lesssim 2 \times 10^7$ K significantly lower than those implied by the X-ray continuum of SN 2023ixf are needed, or, alternatively, a medium with 5–10 times solar metallicity (which we consider unlikely given the metallicity inference of $0.95\,Z_\odot$ by E. A. Zimmerman et al. 2024). A clumpy CSM, with the Fe Kα line formed inside the higher-density clumps (i.e., a multiphase plasma), can explain the observation of the prominent Fe Kα line emission and a very hot continuum, as has been invoked for other strongly interacting SNe (Y. Kohmura et al. 1994; J. C. Houck et al. 1998; S. Uno et al. 2002; V. V. Dwarkadas et al. 2010; P. Chandra et al. 2012; R. Margutti et al. 2017; D. Brethauer et al. 2022). In this scenario, a lower shock temperature can be associated with a slower shock velocity inside clumps. Assuming approximate pressure balance between the clumps and the background medium and for $T \propto v_{sh}^{1/2}$, clumps with density $\rho_c \sim (T_{shock}/T_{clump})\rho_{CSM} \approx 25\rho_{CSM,sh}$ (where $\rho_{CSM,sh}$ is the density of the medium that produces the X-ray continuum) would satisfy the temperature requirement to produce Fe emission. Interestingly, $\rho_c$ is comparable to the density enhancement required by the $NH_{int}$ and density analysis, and it is closer to the density of the optical/UV line forming region (Section 6.2).

Finally, we comment on the evolution of the Fe Kα emission (Table 2). The evolution from an unresolved neutral Fe Kα line to a much broader, resolved spectral feature is consistent with the increasing level of ionization of the CSM (i.e., Fe atoms at different ionization stages contribute to the detected Kα line complex at later times).

### 4.3. Self-consistency Checks

In this subsection, we first discuss the expected signature of inverse Compton (IC) emission on the X-ray spectrum and the nature of the RS and FS in SN 2023ixf (i.e., radiative versus nonradiative) that follow from the properties of the medium inferred above, and we demonstrate that the picture of a FS-dominated thermal X-ray emission is self-consistent. We then address the measured versus expected FS electron temperatures under different physical scenarios.

### 4.4. Inverse Compton Emission and Shock Microphysical Parameters

Nonthermal X-ray emission in SNe can originate from the upscattering of photospheric optical/UV photons off of relativistic electrons accelerated at the FS through IC processes (e.g., C.-I. Björnsson & C. Fransson 2004; R. A. Chevalier et al. 2006). Scattering from a population of nonthermal electrons[37] with energies $E = \gamma_e m_e c^2$ (where $\gamma_e$ is the electron Lorentz factor) distributed as $dN/dE \propto E^{-p}$ generates emission with a spectrum $F_\nu \propto \nu^{-(p-1)/2}$ in the optically thin regime. The normalization of the resulting IC spectrum further depends on the properties of the seed photons (i.e., photospheric temperature $T_{ph}$ and SN bolometric luminosity $L_{bol}$), as well as on the post-shock energy fraction in relativistic electrons $\epsilon_e$, the CSM density $\rho_{CSM}$, and the shock velocity $v_{sh}$.

We adopt the IC formalism of R. Margutti et al. (2012) modified to (i) accommodate a shock velocity $v_{sh} \propto t^{-\alpha}$ with $\alpha \approx 0.1$ (as expected for a massive stellar progenitor star and a wind-like CSM density profile, R. A. Chevalier 1982) with a normalization chosen to give an average shock velocity of ∼10,000 km s$^{-1}$ in the first ∼200 days of evolution as found from VLBI observations of SN 2023ixf (M. Bietenholz 2025, private communication); (ii) we also include the effects of IC cooling.

We use the $L_{bol}$ and $T_{ph}$ estimates from E. A. Zimmerman et al. (2024), and we adopt $p = 3$ as typically inferred for radio SNe (e.g., A. M. Soderberg et al. 2005; R. A. Chevalier et al. 2006; A. M. Soderberg et al. 2010), and consistent with the updated predictions of nonlinear diffusive shock acceleration (DSA) of particles (R. Diesing & D. Caprioli 2021). A harder electron distribution with $p \approx 2$ (as expected from classical DSA theory in the test particle limit; e.g., D. Caprioli 2023 and references therein) would lead to the same conclusions. The luminous $L_{bol}$ of SN 2023ixf implies that during the first ≈week, the electron population is effectively cooling through IC emission (discussed in more detail in Section 5.3). After accounting for IC cooling, we find the resulting IC $L_X \ll 10^{40}$ erg s$^{-1}$ at all times for all physical choices of $\epsilon_e$ values and for the CSM densities of interest. This result is consistent with the lack of observational evidence of any nonthermal X-ray component in our spectra. However, it also leaves the parameter space of shock microphysical parameter values entirely unconstrained. In the radio/X-ray SN literature, equipartition with $\epsilon_e \approx 0.1$ is often assumed but without strong

[37] We do not consider here the X-ray emission from the IC scattering by the thermal electron population of electrons as this component tends to be important only for $T_e > 10^9$ K (C. Fransson et al. 1996).

observational support. The analysis of data from some Galactic SN remnants (e.g., S. K. Sarbadhicary et al. 2017; S. P. Reynolds et al. 2021 and references therein) favor significantly lower values[38] $\epsilon_e \lesssim 0.5 \times 10^{-3}$, in line with the theoretical expectations from nonlinear DSA at nonrelativistic shocks (J. Park et al. 2015; S. Gupta et al. 2024). In the following, we adopt $\epsilon_e = 10^{-4}$ when needed (see also K. Murase et al. 2014, for the similar argument), and we comment on the implications of this assumption where relevant.

#### 4.4.1. Radiative Versus Adiabatic Shocks

At $T_e \gtrsim 2.6 \times 10^7$ K free–free continuum emission dominates the cooling, and the cooling timescale derived from G. B. Rybicki & A. P. Lightman 1979, their Equation (5.15b), is:

$$t_{ff} \approx 1.5 \times 10^{11} \left( \frac{T_e^{1/2}}{n_I \overline{g_{ff}} \mathcal{Z}^2} \right) \mathrm{s}, \quad (4)$$

where $\overline{g_{ff}}$ is the velocity averaged Gaunt factor and $\mathcal{Z}$ is the charge (effectively, the average number of free electrons per ion in the plasma, i.e., $\approx n_e/n_I = \mu_I/\mu_e$). For the electron temperatures measured in SN 2023ixf and our inferred densities, we find that $t_{ff} \geqslant t_{\rm dyn}$ at all times of our monitoring. We note that IC losses are also not important at $\delta t \geqslant 8$ days, given the optical–UV bolometric luminosity of SN 2023ixf from E. A. Zimmerman et al. (2024). We thus conclude that the FS is adiabatic at $\delta t \geqslant 8$ days and that single-temperature spectral modeling is likely adequate (as opposed to radiative shocks where the spectrum can be formed in gas zones with very different temperatures; T. K. Nymark et al. 2006).[39] It follows that at $\delta t \geqslant 4$ days, the FS X-ray luminosity does not track the shock kinetic luminosity, i.e., the relation $L_{\rm X} = (4\pi R_{\rm sh}^2) \times \frac{1}{2}\rho_{\rm sh} v_{\rm sh}^3$ used by E. A. Zimmerman et al. (2024) does not apply, and the derived inferences are not physical.

Adopting the shock jump conditions for a strong shock in the thin shell approximation, the density of the shocked ejecta behind the RS is much higher than the density of the shocked CSM behind the forward shock (e.g., C. Fransson et al. 1996, their Equation (3.3):

$$\rho_{\rm RS} = \frac{(n-3)(n-4)}{(3-s)(4-s)} \times \rho_{\rm FS} \overset{s=2,n=12}{=} 144 \times \rho_{\rm FS}. \quad (5)$$

The larger density and lower temperature of the RS region (Equation (2)) imply significantly smaller free–free cooling times. From Equation (4), we find $t_{ff} \leqslant 0.1 t_{\rm dyn}$ for the RS at all times of our monitoring, from which we conclude that the RS is radiative.[40] We note that the radiative nature of the RS is independently supported by the detection of the H$\alpha$ line with a boxy profile (R. A. Chevalier & C. Fransson 1985) in the optical spectra of SN 2023ixf (R. S. Teja et al. 2023). Radiative cooling of the RS and the thermal instabilities that may occur as a consequence lead to the formation of a cold dense shell (CDS) close to the contact discontinuity between the two shocked regions (e.g., C. Fransson 1984; R. A. Chevalier & C. Fransson 1985). The CDS provides a time-dependent photoelectric absorption component that is able to efficiently obscure the entire X-ray emission from the RS, as we show below.

The column density of the CDS gas is $N_{\rm CDS}(t) \approx \frac{M_{\rm RS}(t)}{4\pi R(t)_{\rm sh}^2 \mu m_p}$, where $M_{\rm RS}(t)$ is the ejecta mass that has crossed the RS at a given time $t$, $\mu$ is the mean mass per particle (i.e., ions and free electrons) behind the RS, and $m_p$ is the proton mass (e.g., T. K. Nymark et al. 2006, their Equation (50)). In the self-similar regime of R. A. Chevalier (1982), thin shell approximation, $M_{\rm RS} = \frac{(n-4)}{(4-s)} M_{\rm FS}$, where $M_{\rm FS}$ is the mass of the shocked CSM. For $s \approx 2$, $v_{\rm sh} \approx 10^4$ km s$^{-1}$ and the CSM density inferred in Section 4.1 we find $N_{\rm CDS}(t) \approx \frac{10^{25}}{(t/\mathrm{d})}$ cm$^{-2}$ (e.g., R. A. Chevalier & C. Fransson 2017, their Equation (17)), which implies $N_{\rm CDS} \gtrsim 10^{23}$ cm$^{-2}$ at $\delta t < 85$ days and a photoelectric absorption optical depth $\tau_{\rm phot} > 1$ for photons with energy $E \lesssim 3$ keV at all times of our monitoring (while observed spectra clearly have emission below 3 keV, Figure 5). Finally, adopting the RS luminosity formulation by C. Fransson et al. (1996), their Equation (3.10), self-consistently corrected for the photoelectric absorption term calculated above, we predict that the observed RS X-ray luminosity might become comparable to the FS emission at $\delta t \gtrsim 100$ days, potentially leading to a flattening of the X-ray light curve. We conclude that the RS X-ray emission is effectively absorbed by the CDS at $\delta t < 85$ days and that the detected emission from SN 2023ixf is from the FS material, consistent with our assumptions above.

#### 4.4.2. Electron–Ion Equipartition

Next, we address the question of the low electron temperatures $T_e$ compared to the expectations from shock dynamics and shock jump conditions of Equation (1). The timescale for Coulomb equipartition between electrons and ions in the shocked region is (Equation (12) of R. A. Chevalier & C. Fransson 2017):

$$t_{e-i,\rm eq} \approx 2.5 \times 10^7 \left( \frac{n_e}{10^7\ \mathrm{cm}^{-3}} \right)^{-1} \left( \frac{T}{10^9\ \mathrm{K}} \right)^{1.5} \mathrm{s} \quad (6)$$

(L. Spitzer 1978; S. Stepney 1983). It follows that for the densities of the shocked CSM inferred above[41] $t_{e-i,\rm eq} \approx t_{\rm dyn}$ at $\delta t \leqslant 10$ days, at which time the electrons are marginally in equipartition, with electrons falling more and more out of equilibrium with time as the density drops with radius. Ion-electron collisions are thus ineffective, and we expect $T_e < T_i$ at the FS. We measure $k_b T_e \leqslant 30$ keV at $\delta t \geqslant 20$ days, which is lower than the ion temperature $k_b T_i \approx 100$ keV from Equation (1), consistent with this expectation. Parenthetically, this result also implies that plasma instabilities are also inefficient in heating the electrons collisionlessly.

[38] We caution that Galactic SNR shocks are significantly slower ($v_{\rm sh} \leqslant 0.01c$; e.g., H. Zeng et al. 2019) and might therefore probe a different regime of shock particle acceleration than young shocks in Type IIP SNe.

[39] The same conclusion would be reached by using the $t_{ff}$ relation provided by R. A. Chevalier & C. Fransson (2017).

[40] Equation (4) only includes free–free cooling. Line emission, which becomes important at $T_e \lesssim 2.6 \times 10^7$ K, would further increase the cooling rate (e.g., R. A. Chevalier & C. Fransson 2017, their Equation (15)), thus reinforcing our conclusions of a radiative RS.

[41] For a strong shock in a gas with adiabatic index $\gamma_{\rm ad} = 5/3$, $\rho_{\rm sh,CSM} = 4\rho_{\rm CSM}$).

## 5. Inferences from Radio Observations

### 5.1. Radio Spectral Modeling and Physical Parameters

We model the radio spectra of SN 2023ixf at each epoch with a smoothed broken-power-law (BPL) function (A. M. Soderberg et al. 2006) of the form:

$$F_\nu = F_{\rm pk}\left[\left(\frac{\nu}{\nu_{\rm pk}}\right)^{\alpha_1/s} + \left(\frac{\nu}{\nu_{\rm pk}}\right)^{\alpha_2/s}\right]^s. \quad (7)$$

Here, $\alpha_2$ represents the optically thick spectral index of the synchrotron self-absorbed (SSA) spectrum. We expect $\alpha_2 = 5/2$ if the SSA peak ($\nu_{\rm SSA}$) is greater than the characteristic synchrotron frequency ($\nu_{\rm m}$). $\alpha_1$ is the optically thin spectral index, which is related to the electron power-law index $p$ as $\alpha_1 = -(p-1)/2$, where the electron energy power-law distribution is $dN(E)/dE = N_0 E^{-p}$. The smoothing parameter $s$ determines the sharpness of the transition from the optically thick to the optically thin phase. $\nu_{\rm pk}$ and $F_{\rm pk}$ represent the frequency and flux density at which the optically thick and thin power laws of the SSA spectrum intersect.

We fit the BPL model to each of the spectra, treating $\alpha_2$, $\nu_{\rm pk}$, and $F_{\rm pk}$ as free parameters, fixing $s = -1$. Since the optically thin phase of the spectra is not well sampled, we impose the optically thin spectral index to be $\alpha_1 = -1$ ($p = 3$). The best-fit parameters are listed in Table 3, and the best-fit modeled spectra are presented in Figure 1.

The spectra are well-represented by an SSA model with optically thick spectral indices varying from $\alpha_2 = 2.4 \pm 0.1$ to $2.9 \pm 0.2$. These values broadly agree with the theoretical value of $5/2$ within error bars. The peak frequencies cascade to lower values at later epochs with a temporal index of $\nu_{\rm pk} \propto t^{-0.78 \pm 0.03}$. The peak flux density increases as $F_{\rm pk} \propto t^{1.34 \pm 0.21}$. We note that the NOEMA 84 GHz flux density measurement at $\delta t \approx 38$ days (purple star symbol in Figure 1) is significantly above the near-simultaneous SED at $\delta t \approx 33$ days and even the SED at $\delta t \approx 57$ days. Also, the 84 GHz flux density at $\delta t \approx 23$ days is above the modeled SED at $\delta t \approx 33$ days, which is contradictory to the temporal evolution of SEDs. We address this further in Sections 5.5 and 5.6.

In a standard SSA scenario, for a wind-like CSM, $F_{\rm pk}$ remains constant for $m = 1$ and decreases with time for smaller values of $m$ (R. A. Chevalier 1998), where $m$ is the shock deceleration parameter defined as $r \propto t^m$. The radio spectra of SN 2023ixf evolve as $F_{\rm pk} \propto t^{1.34 \pm 0.21}$ and do not follow this trend. Even though the optically thin evolution is not well sampled, it is clear that the optically thin flux also increases from $\delta t = 33$–$89$ days with an average index of $F_{\rm thin} \propto t$, remaining roughly constant between $\delta t = 89$–$165$ days. Optically thin synchrotron flux densities scale as $F_{\rm thin} \propto R^3 N_0 B^{\frac{p+1}{2}}$, where $N_0 \propto B^2$ if the energy density of relativistic electrons is a constant fraction ($\epsilon_e$) of shock energy density ($\rho_{\rm CSM} v^2$). In that case, the observed temporal evolution of optically thin flux densities indicates a CSM density profile shallower than that created by a steady stellar wind. We further explore the CSM density profile by detailed modeling of radio SEDs in Section 5.2.

The best-fit $\nu_{\rm pk}$ and $F_{\rm pk}$ from the SSA spectrum can constrain shock radii, velocities, and magnetic fields at multiple epochs post-explosion (R. A. Chevalier 1998). We use Equations (13) and (14) from R. A. Chevalier (1998) and assume $\epsilon_e = \epsilon_B$ to estimate $R$, $v$, and $B$ at $\delta t = 33$, 57, 89, and 165 days, and the values are presented in Table 3. The mean shock velocities are $v = 1582 \pm 178$–$2716 \pm 280\,{\rm km\,s^{-1}}$, significantly lower than the velocities derived from optical line measurements ($v \sim 8400\,{\rm km\,s^{-1}}$) at $\delta t \approx 2.4$–$14.4$ days (W. V. Jacobson-Galán et al. 2023).

**Table 3**
Shock Parameters of SN 2023ixf Estimated from Single-epoch Radio SED Modeling Using a BPL Function

| Time[a] (days) | $\alpha_2$ | $\nu_{pk}$[b] (GHz) | $F_{pk}$[b] ($\mu$Jy) |
|---|---|---|---|
| 33 | $2.8 \pm 0.3$ | $17.6 \pm 1.0$ | $565 \pm 25$ |
| 57 | $2.4 \pm 0.1$ | $12.3 \pm 0.4$ | $998 \pm 16$ |
| 89 | $2.9 \pm 0.2$ | $8.7 \pm 0.2$ | $2387 \pm 40$ |
| 165 | $2.4 \pm 0.2$ | $5.2 \pm 0.2$ | $3998 \pm 107$ |

**Notes.**
[a] With respect to the date of the explosion.
[b] $\nu_{\rm pk}$ and $F_{\rm pk}$ are the intersection of the optically thick and thin power laws of the synchrotron spectrum.

An SN ejecta of mass $M_{\rm ej} \approx 1\,M_\odot$ can be decelerated from $8400\,{\rm km\,s^{-1}}$ to $\approx 1600\,{\rm km\,s^{-1}}$ by a CSM of mass $\approx 4\,M_\odot$. However, a large fraction of ejecta kinetic energy ($\approx \frac{M_{\rm csm}}{M_{\rm ej}+M_{\rm csm}}$) will be dissipated in such an interaction, which is not observed in the case of SN 2023ixf. Additionally, such a CSM mass would result in a density $\approx 10^{-13}\,{\rm g\,cm^{-3}}$ at radius $R < 3 \times 10^{15}$ cm, resulting in very high free–free optical depth ($\tau_{\rm FFA} >> 1$), resulting in nondetection at all the observed VLA frequency bands at $\delta t \approx 33$ days. Thus, the very small shock velocities inferred from the SSA model are not correct. We explore alternative scenarios below.

### 5.2. Simultaneous Fit to Multiepoch SEDs

Shock velocities derived from the SSA formulation above could be lower limits if free–free absorption (FFA) determines the observed peak of the SED. In this case, the actual SSA peak would be at much lower frequencies. Here, we attempt to simultaneously model the multiepoch SEDs under the following assumptions: (1) The blast wave is expanding at a velocity of $\sim$10,000 km s$^{-1}$. (2) The density of the CSM is $\rho_{\rm CSM}(r) = \rho_0(\frac{1}{r^s})$ with electron temperature $T_e$ up to the shock radius at $\delta t \approx 165$ days. (3) The CSM outside this radius is wind-like, and the FFA optical depth due to this medium at 1 GHz is $\tau_{\rm out}$. We use the BPL functional form multiplied with $e^{-\tau_{\rm FFA}}$ to implement FFA (i.e., BPL $\times$ e$^{-\tau_{\rm FFA}}$). The $\nu_{\rm pk}$ (GHz) and $F_{\rm pk}$ (Jy) are defined as functions of $R$ and $B$ following R. A. Chevalier (1998) for $p = 3$.

$$F_{\rm pk} = \left[\left(\frac{\rm RB}{5.046 \times 10^{15}}\right)\left(\frac{\epsilon_e}{\epsilon_B}\right)^{\frac{5}{19}}\left(\frac{D}{\rm Mpc}\right)^{\frac{-14}{19}}\right]^{\frac{19}{7}}, \quad (8)$$

$$\nu_{\rm pk} = \left[3.801 \times 10^{17}\left(\frac{\epsilon_e}{\epsilon_B}\right)^{\frac{3}{19}} F_{\rm pk}^{\frac{11}{19}}\left(\frac{D}{\rm Mpc}\right)^{\frac{22}{19}}\left(\frac{R}{B}\right)^{-1}\right]^{0.5}. \quad (9)$$

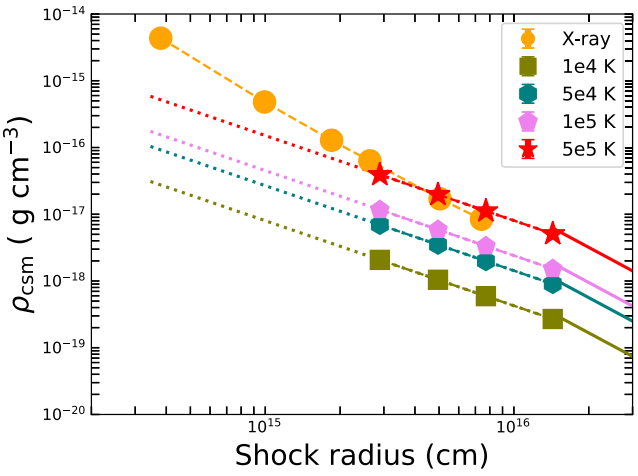


**Figure 8.** CSM density profiles for various CSM temperatures obtained from multiepoch radio SED modeling. The star symbols denote the densities at the epoch of radio observations: $t \approx 33$, 57, 89, and 165 days, and the solid lines represent the wind-density profiles beyond the shock radius at $t \approx 165$ days, estimated from the $\tau_{out}$ parameter. The dotted lines are extrapolations of the radio-derived CSM density profiles to earlier epochs.

The FFA optical depth is given by G. B. Rybicki & A. P. Lightman (1979):

$$\tau_{FFA} = \int_{R}^{\infty} 0.018 \times T_e^{-3/2} Z^2 \nu^{-2} g_{ff}\, n_e\, n_i dr. \quad (10)$$

We use the Gaunt factor $g_{ff} = 5$, charge $Z = 1$, and $n_e = n_i = \rho_{CSM}/m_p$. The free parameters in this physical model are $\epsilon_e$, $\epsilon_B$, $\rho_0$, $s$, $T_e$, and $\tau_{out}$. Here, $\rho_0$ and $s$ are defined such that $\rho_{CSM}(r) = \rho_0 \left(\frac{r}{R_0}\right)^{-s}$, where $R_0$ is the shock radius at $t = 33.45$ days. Initially, we perform MCMC fit to multiepoch SEDs, keeping $\epsilon_e$, $\epsilon_B$, $\rho_0$, $s$, $T_e$, and $\tau_{out}$ as free parameters using the Python package `emcee` (D. Foreman-Mackey et al. 2013). The best-fit values of the parameters are $\epsilon_e = 0.19^{+0.09}_{-0.08}$, $\epsilon_B = 2.04^{+3.37}_{-0.83} \times 10^{-6}$, $T_e = 4.61^{+2.40}_{-2.20} \times 10^5$ K, $\rho_0 = 4.06^{+1.52}_{-1.57} \times 10^{-17}$ g cm$^{-3}$, $s = 1.31^{+0.01}_{-0.01}$, and $\tau_{out} = 14.71^{+0.66}_{-0.65}$. We note from the corner plots that the parameters ($\epsilon_e$, $\epsilon_B$) and ($\rho_0$, $T_e$) are highly correlated based on their covariance.

Next, we attempt the fit for different values of $T_e = 10^4$, $5 \times 10^4$, $10^5$, and $5 \times 10^5$ K to remove the degeneracy between $\rho_0$ and $T_e$ from the modeling. We allow $\epsilon_e$, $\epsilon_B$, $\rho_0$, $s$, and $\tau_{out}$ to vary. The solutions result in a range of values for $\epsilon_e \sim$ (0.16–0.21) and $\epsilon_B \sim$ (0.02–6) $\times 10^{-4}$. The best-fit $\rho_0$ strongly depends on the value of $T_e$, resulting in higher $\rho_0$ for higher $T_e$, while $s$ and $\tau_{out}$ remain roughly similar. We show the variation of best-fit $\rho_{csm}$ for different $T_e$ in Figure 8. Interestingly, the densities for the $T_e = 5 \times 10^5$ K model align with the densities derived from the X-ray EM of the previous section. A CSM temperature slightly above $10^5$ K is estimated for SN 1993J at $t >$ 10–15 days post-explosion (C. Fransson et al. 1996), based on modeling the CSM structure using a time-dependent photoionization code (P. Lundqvist & C. Fransson 1991). We thus adopt $T_e = 5 \times 10^5$ K as a fiducial value.

Finally, we fit the model for different values of $\epsilon_e$, fixing $T_e = 5 \times 10^5$ K and allowing $\epsilon_B$, $\rho_0$, $s$, and $\tau_{out}$ to vary. The best-fit solutions are presented in Table 4, with the corresponding spectra shown in Figure 9 and the corner plot in Figure 10. The results show a locus of $\epsilon_e$ and $\epsilon_B$ values that can account for the observed SEDs for a similar density profile. For further analysis and interpretation, we select the solution with $\epsilon_e = 10^{-4}$, based on the argument of Section 4.4. We note that the observed data show optically thick spectral slopes that are flatter than those predicted by the best-fit FFA model. This is likely due to inhomogeneities that soften the optically thick portion of the spectrum, whereas the FFA model assumes a uniform optical depth.

### 5.3. Energy Losses of Nonthermal Electrons

Synchrotron-emitting electrons can lose energy through various processes: synchrotron cooling, IC cooling, and Coulomb cooling. These processes become significant when the energy loss timescales are comparable to or shorter than the dynamical timescale ($t_d$) of the system. The timescales for synchrotron ($t_{sync}$), IC ($t_{IC}$), and Coulomb cooling ($t_{Coul}$) are given by C. Fransson et al. (1996) and R. A. Chevalier & C. Fransson (2017):

$$t_{sync} = 7.74 \times 10^8\, \gamma^{-1} B^{-2} \text{ s}, \quad (11)$$

$$t_{IC} = 1.16 \times 10^{19}\, \gamma^{-1} L_{bol}^{-1} R^2 \text{ s}, \quad (12)$$

$$t_{Coul} = 0.67 \times 10^{-12}\, \gamma \rho_{csm}^{-1} \text{ s}. \quad (13)$$

$L_{bol}$ is the bolometric luminosity of the SN, which includes contributions from both the ejecta and circumstellar interaction. If the intrinsic spectrum of relativistic electrons is $dN(E)/dE = N_0 E^{-p}$, the synchrotron and IC cooling will steepen the distribution of these electrons to $N_0 E^{-p-1}$. Consequently, the synchrotron spectrum will have a steeper spectral index ($F_\nu \propto \nu^{-p/2}$) above a certain frequency, known as the synchrotron/IC cooling frequency ($\nu_{sync}/\nu_{IC}$). This is the characteristic synchrotron emission frequency ($\nu = 1.2 \times 10^6 B\gamma^2$ Hz) of an electron with Lorentz factor ($\gamma$) for which $t_{SC}$ or $t_{IC}$ equals the dynamical timescale. On the other hand, Coulomb losses alter the spectrum in the opposite direction, resulting in a flatter spectral index ($F_\nu \propto \nu^{-p/2+1}$) at frequencies below a characteristic cooling frequency ($\nu_{Coul}$) where $t_{Coul} = t_d$. We caution that the steepening/flattening of the spectrum can be a bit more complicated since it depends on multiple populations of electrons accelerated at different times (R. Diesing & D. Caprioli 2019), and the calculation that we follow here is a simplified treatment.

Depending on the values of $\epsilon_e$, $\epsilon_B$, and the CSM density profile, the cooling frequencies and their evolution across the spectrum will vary. We calculate these cooling frequencies to understand the possible impact of electron cooling on the modeled SEDs and best-fit parameters. We use the magnetic field values from the scaling relation $\frac{B^2}{8\pi} = \epsilon_B\, \rho\, v^2$ to estimate the $\nu_{sync}$. To calculate $\nu_{IC}$, we use the bolometric luminosities from E. A. Zimmerman et al. (2024). Various cooling frequencies for the model with $\epsilon_e = 10^{-4}$ are presented in Table 5.

Except for $t \approx 165$ days, the competing effects of synchrotron/IC cooling and Coulomb cooling could be affecting the observed spectrum, resulting in no clear signature of either. At $t \approx 165$ days, a spectral steepening due to

**Table 4**
Best-fit Parameters Estimated from Multiepoch Radio SED Modeling Discussed in Section 5.2

| $T_e$ (K) | $\epsilon_e$ ... | $\epsilon_B$ ... | $\rho_0$ ($\times 10^{-17}$gm cm$^{-3}$) | $s$ ... | $\tau_{out}$ (at 1 GHz) | $B$ ($\delta t$ = 33, 57, 89, 165 days) (Gauss) |
|---|---|---|---|---|---|---|
| $5 \times 10^5$ | 0.1 | $3.42^{+0.08}_{-0.07} \times 10^{-6}$ | $3.91^{+0.08}_{-0.08}$ | $1.27^{0.01}_{-0.01}$ | $16.70^{+1.07}_{-1.05}$ | 0.058, 0.041, 0.031, 0.021 |
| $5 \times 10^5$ | 0.01 | $3.43^{+0.08}_{-0.07} \times 10^{-5}$ | $3.89^{+0.08}_{-0.08}$ | $1.27^{0.01}_{-0.01}$ | $16.20^{+1.05}_{-1.04}$ | 0.183, 0.130, 0.098, 0.066 |
| $5 \times 10^5$ | 0.001 | $3.46^{+0.08}_{-0.07} \times 10^{-4}$ | $3.86^{+0.08}_{-0.08}$ | $1.27^{0.01}_{-0.01}$ | $15.40^{+1.05}_{-1.04}$ | 0.579, 0.412, 0.311, 0.210 |
| $5 \times 10^5$ | 0.0001 | $3.52^{+0.08}_{-0.08} \times 10^{-3}$ | $3.82^{+0.08}_{-0.08}$ | $1.27^{0.01}_{-0.01}$ | $14.10^{+1.05}_{-1.04}$ | 1.838, 1.306, 0.985, 0.665 |
| $5 \times 10^5$ | $10^{-5}$ | $3.61^{+0.09}_{-0.08} \times 10^{-2}$ | $3.74^{+0.08}_{-0.08}$ | $1.27^{0.01}_{-0.01}$ | $12.00^{+1.05}_{-1.04}$ | 5.825, 4.138, 3.123, 2.108 |

**Note.** $T_e$ is the CSM electron temperature. $\epsilon_e$ and $\epsilon_B$ are the fractions of shock energy fed into relativistic electrons and magnetic fields, respectively. $\rho_0$ and $s$ are defined such that $\rho_{CSM}(r) = \rho_0\left(\frac{r}{R_0}\right)^{-s}$, where $R_0$ is the shock radius at $\delta t = 33.45$ days. $\tau_{out}$ is the FFA optical depth at 1 GHz due to the medium outside the shock radius at $\delta t = 165.78$ days. The listed parameters are obtained by fitting the model, fixing $T_e$ and $\epsilon_e$, and keeping $\epsilon_B$, $\rho_0$, $s$, and $\tau_{out}$ as free parameters. $B$ is the magnetic field estimated using the scaling relation $\frac{B^2}{8\pi} = \epsilon_B \rho_{CSM}(r) v^2$.

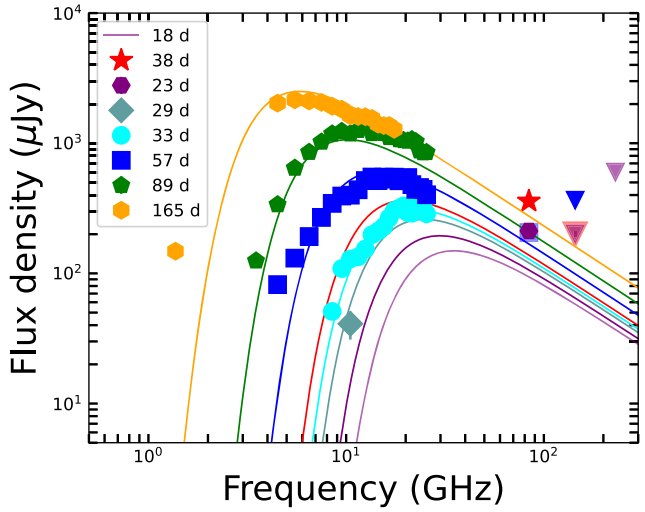


**Figure 9.** Best-fit radio spectral energy distributions of SN 2023ixf along with observed flux measurements in the time range $\delta t$ = 33–165 days. Inverted triangles mark the $5\sigma$ flux density upper limits. The parameters are obtained by fitting the model, fixing $T_e = 5 \times 10^5$ K and $\epsilon_e = 10^{-4}$, and keeping $\epsilon_B$, $\rho_0$, $s$, and $\tau_{out}$ as free parameters.

synchrotron cooling is expected at $\nu \approx 12$ GHz. Although our observations do not adequately cover the optically thin phase of evolution, there is no evident spectral steepening in any of the spectra. We compute the cooling frequencies for the model with $\epsilon_e = 10^{-5}$ and find that there is synchrotron and/or IC cooling at frequencies >0.4 GHz and Coulomb cooling at frequencies <29 GHz. However, as mentioned previously, these effects could cancel each other out.

To summarize, cooling processes can modify the intrinsic SSA from what is defined by Equations (8) and (9). Ideally, one needs to systematically incorporate all the cooling losses in the electron distribution and model the radio emission (C. Fransson & C.-I. Björnsson 1998). However, since FFA dominates the absorption, our density estimates from radio modeling are not significantly impacted by the shape of intrinsic SSA. We quantitatively address this in Section 5.4.

### 5.4. CSM Densities from FFA Model

The density of the CSM can be estimated by fitting an FFA-only model to each of the spectra. In this approach, the derived densities are agnostic about the shape of the intrinsic synchrotron spectrum. We model the single-epoch SEDs with

**Table 5**
Cooling Frequencies That Correspond to the Best-fit Parameters from Multiepoch Radio SED Modeling Listed in Table 4 for $\epsilon_e = 10^{-4}$

| Time (days) | $\nu_{sync}$ (GHz) | $\nu_{IC}$ (GHz) | $\nu_{Coul}$ (GHz) | $\nu_{SSA}$ (GHz) | $\nu_{peak}$ (GHz) |
|---|---|---|---|---|---|
| 33.45 | 14 | 0.3 | 65 | 6 | 22 |
| 57.31 | 13 | 1 | 34 | 4 | 15 |
| 89.30 | 13 | 28 | 20 | 4 | 10 |
| 165.78 | 12 | 248 | 10 | 2 | 6 |

**Note.** $\nu_{sync}$, $\nu_{IC}$, and $\nu_{Coul}$ are cooling frequencies due to synchrotron, IC, and Coulomb losses. $\nu_{SSA}$ is the synchrotron self-absorption frequency. At $\nu > \nu_{IC}$, IC cooling is important, and at $\nu > \nu_{sync}$, synchrotron cooling is important, whereas Coulomb cooling becomes important at $\nu < \nu_{Coul}$. $\nu_{peak}$ is the observed peak of the SED defined by free–free absorption.

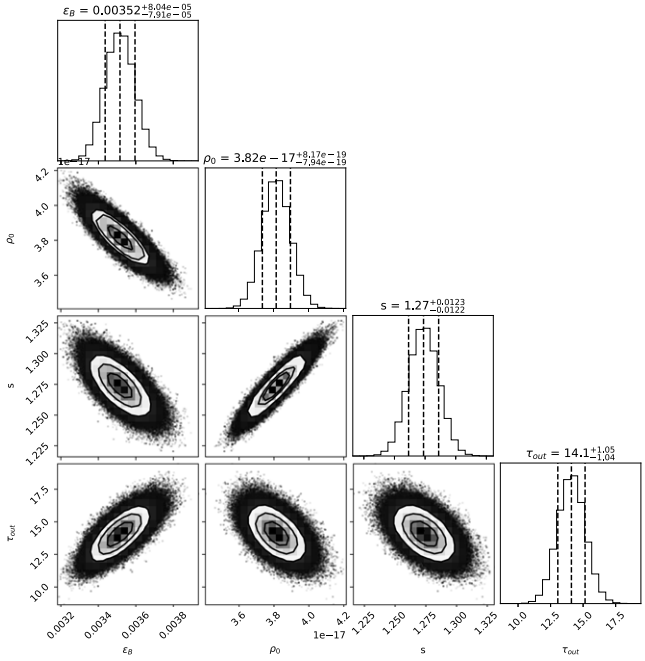


**Figure 10.** Corner plot showing the results of our MCMC fitting of multiepoch radio SEDs (Figure 9) of SN 2023ixf (see Section 5.2 for details). $\epsilon_B$ is the fraction of shock energy fed into the magnetic fields. $\rho_0$ and $s$ are defined such that $\rho_{CSM}(r) = \rho_0\left(\frac{r}{R_0}\right)^{-s}$, where $R_0$ is the shock radius at $\delta t = 33.45$ days. $\tau_{out}$ is the FFA optical depth at 1 GHz due to the medium outside the shock radius at $\delta t = 165.78$ days. The corner plot is obtained by fitting the model, fixing $T_e = 5 \times 10^5$ K and $\epsilon_e = 10^{-4}$ and keeping $\epsilon_B$, $\rho_0$, $s$, and $\tau_{out}$ as free parameters. In each panel, the 16, 50, and 84 percentiles are marked.

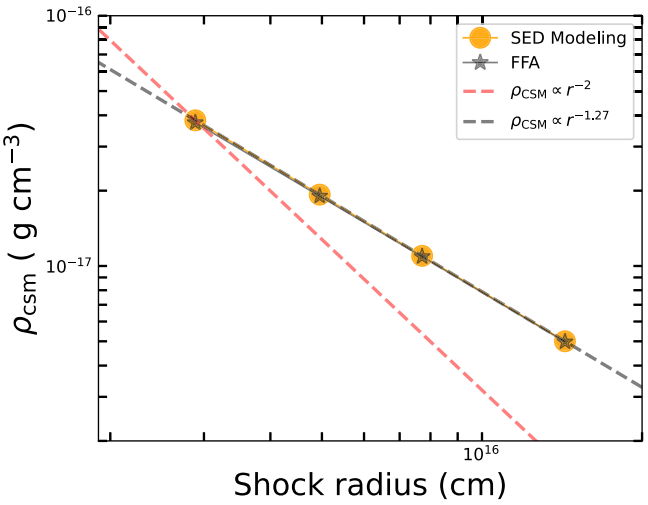


**Figure 11.** Best-fit CSM densities of SN 2023ixf derived from multiepoch radio SED modeling (orange circles) and from single-epoch FFA-only fits (black star symbols). Dashed red and black lines are to guide the eye and denote a reference wind-density profile $\rho_{CSM}(r) \propto r^{-2}$ and $\rho_{CSM}(r) \propto r^{-1.3}$, respectively.

the FFA model of the form:

$$F_\nu = K_1\left(\frac{\nu}{5\ \mathrm{GHz}}\right)^{\beta} \exp\left[-K_2\left(\frac{\nu}{5\ \mathrm{GHz}}\right)^{-2.1}\right]. \quad (14)$$

Here, $K_1$ and $K_2$ are flux density and optical depth normalization constants, respectively. $\beta$ is the optically thin spectral index. We fix $\beta = -1$ and fit the function, allowing $K_1$ and $K_2$ to vary as free parameters for each spectrum.

We use the $\tau_{FFA}$ (5 GHz) to fit for the CSM density profile following Equation (10) assuming $T_e = 5 \times 10^5$ K. The best-fit density profile is $\rho_{CSM}(r) = \rho_0\left(\frac{r}{R_0}\right)^{-1.26^{+0.01}_{-0.01}}$, where $\rho_0 = 3.74^{+0.10}_{-0.10} \times 10^{-17}$ g cm$^{-3}$ for the shock radius at $\delta t = 33.45$ days. This density is consistent with the densities derived from multiepoch radio modeling for the range of $\epsilon_e = 0.1$–$10^{-5}$. Figure 11 shows a comparison between CSM densities derived by modeling multiepoch radio SEDs for $\epsilon_e = 10^{-4}$ and that from single-epoch FFA fits.

### 5.5. Early Radio Upper Limits

Multiepoch ($\delta t \approx 33$–165 days) radio SED modeling favors a CSM density profile $\rho_{CSM}(r) \propto r^{-1.3}$, whereas the densities derived from X-ray observations ($\delta t \approx 4$–86 days) follow a density profile $\rho_{CSM}(r) \propto r^{-2}$. Either both density regions coexist in the regions probed by these observations, or there is a transition from $\rho_{CSM} \propto r^{-2}$ to $\rho_{CSM} \propto r^{-1.3}$ from smaller to larger shock radii. To check this, we simulate the radio SEDs that could arise from the X-ray emitting plasma for $\epsilon_e = 10^{-4}$ and $\epsilon_B = 3.52 \times 10^{-3}$ (see Figure 12). We also extrapolate the best-fit radio model in time to earlier epochs covering the X-ray observation epochs. Additionally, we place the early-time ($\delta t \approx 2$–18 days) radio flux density upper limits from the literature (E. Berger et al. 2023) on these two sets of SEDs. At $\delta t \approx 2$–18 days, the radio upper limits are consistent with both sets of SEDs. At $\delta t \approx 23$ days, the SED from X-ray emitting plasma is above the 84 GHz NOEMA flux density by a factor of $\approx$2. At times $\delta t > 23$ days, the SEDs from X-ray emitting plasma overpredict the observed radio flux densities in the optically thick regime (see cyan curve for $\delta t \approx 33$ days in Figure 12). The model flux at $\delta t \approx 38$ and 62 days are roughly consistent with the predictions from the radio SEDs from X-ray-emitting plasma (red and blue circles at 84 GHz). It is likely that a $\rho_{CSM}(r) \propto r^{-1.3}$ profile is dominant at radii corresponding to $\delta t \gtrsim 23$ days. However, the extrapolated radio SEDs at $\delta t \approx 23$ and 38 days underpredict the 84 GHz NOEMA fluxes. We explore the possibility of contribution from secondary electrons and positrons to address this in Section 5.6.

The flatter density profile from radio SED modeling can be interpreted in two ways. One, the corresponding stellar evolution phase has either varying $\dot{M}$ or $v_w$. Two, the CSM is clumpy and nonspherically symmetric. If the clumpy CSM has a filling factor $f_{cl}$, the free–free optical depth will be $\tau_{FFA} \propto \int f_{cl} n_e n_i dr$ (C. Fransson et al. 1996). If the $f_{cl}$ varies with radius ($f_{cl} \propto r^{1.5}$), a wind-density CSM profile can result in the observed radio SEDs.

### 5.6. Radio Emission from Secondary Leptons Produced by Cosmic-Ray Protons

Efficient cosmic-ray (CR) proton acceleration can happen when the SN ejecta interacts with dense CSM, and the shock becomes radiation unmediated (K. Murase et al. 2011; B. Katz et al. 2012; K. Murase 2018). The accelerated protons undergo $pp$ collisions and produce gamma rays, neutrinos, and secondary electron–positron pairs. These secondary leptons can produce synchrotron emission detectable at high radio frequencies (K. Murase et al. 2014; M. Petropoulou et al. 2016; K. Murase 2024). In SN 2023ixf, we note that the 84 GHz flux densities at $t \approx 23$ and 38 days are well above the modeled SEDs (see Figure 9). Given that the energy fraction carried by CR protons, $\epsilon_p \sim 0.1$, is larger than that of electrons, $\epsilon_e \sim 10^{-4}$, the secondary emission could be more prominent when $\epsilon_e \lesssim 0.2\epsilon_{p,-1} \min[1, f_{pp}]$, where $f_{pp} \simeq 2.7 \times 10^{-2}\ \rho_{CSM,-16.5} R_{15.5} v_{sh,9}^{-1}$ is the efficiency of inelastic $pp$ interactions. Indeed, the NOEMA flux at $t \approx 23.0$ and 38.2 days are higher than the expectation of the best-fit radio SED model that can be compatible with primary electron acceleration. Thus, we explore the possibility of a contribution from the secondary electron–positron population toward the synchrotron emission at these epochs, adopting the formulation from K. Murase et al. (2014).

The magnetic field strength is estimated to be $B \simeq 1.6$ G $\epsilon_{B,-2.5}^{1/2} \rho_{CSM,-16.5}^{1/2} v_{sh,9}$ (see also Table 4). Noting that the secondary pairs are injected at $\gamma_h \sim 68$ instead of $\gamma_{inj}$ for primary electrons, the characteristic frequency of hadronically injected electrons is given by

$$\nu_h \approx \frac{3}{4\pi}\gamma_h^2 \frac{eB}{m_e c} \simeq 30\ \mathrm{GHz}\ \epsilon_{B,-2.5}^{1/2} \rho_{CSM,-16.5}^{1/2} v_{sh,9}, \quad (15)$$

and the critical frequency determined by radiative (synchrotron or IC) cooling is

$$\nu_{rc} \simeq 0.76\ \mathrm{GHz}\ [(1+Y)/9]^{-2} \epsilon_{B,-2.5}^{-3/2} \rho_{CSM,-16.5}^{-3/2} R_{15.5}^{-2} v_{sh,9}^{-1}, \quad (16)$$

where $Y$ is introduced as

$$Y \approx \frac{2L_{bol}}{R^2 c B^2} \simeq 8.2\quad L_{bol,42.5} \epsilon_{B,-2.5}^{-1} \rho_{CSM,-16.5}^{-1} R_{15.5}^{-2} v_{sh,9}^{-2} \quad (17)$$

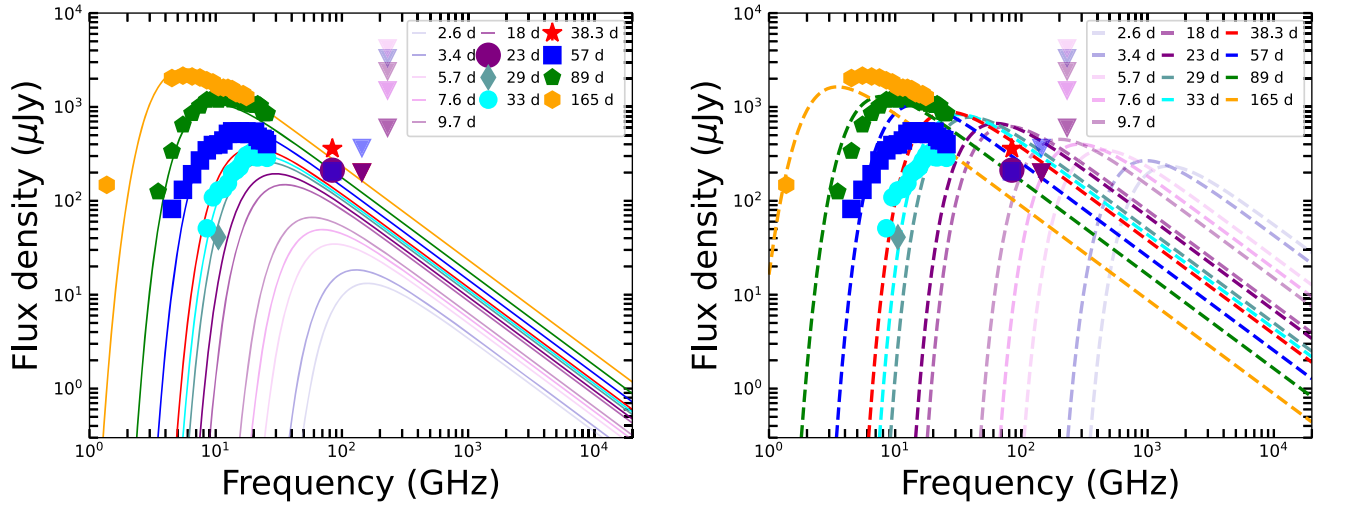


**Figure 12.** Left panel: best-fit radio SEDs from the multiepoch spectral analysis presented in Section 5.2 for a CSM density profile $\rho_{\rm CSM}(r) \propto r^{-1.3}$ extrapolated to earlier times. Right panel: expected radio SEDs that could arise from X-ray emitting plasma for a CSM density profile $\rho_{\rm CSM}(r) \propto r^{-2}$. In both panels, the symbols denote the same epoch of observations.

in the limit that the system is optically thin to Thomson scattering. We estimate $\nu_h$ at $\delta t \approx$ 23.0, 38.2, and 62.04 days, assuming a shock velocity of 10,000 km s$^{-1}$ and $\epsilon_{\rm B} = 3.52 \times 10^{-3}$. Then, the characteristic frequency of secondary electrons and positrons are $\nu_h \sim 45$, 33, and 24 GHz at $\delta t \approx 23$, 38, and 62 days. Note that $\nu_{\rm rc} \approx \min[\nu_{\rm sync}, \nu_{\rm IC}]$ (see Table 5). Thanks to the IC cooling, we find $\nu_{\rm rc} \ll \nu_h$, i.e., the system at early times is in the fast cooling regime (K. Murase 2024), in which the spectrum of electrons and positrons should be extended to energies below $\gamma_h$.

K. Murase (2024) presented calculations of radio emission from secondary electrons and positrons, including Coulomb losses and free–free absorption, and showed that the predicted radio fluxes of SN 2023ixf at $\delta t \approx$ 20–30 days can be $F_\nu \sim$ 10–100 $\mu$Jy for $\dot{M} \sim$ a few $\times 10^{-4}\,M_\odot$ yr$^{-1}$. Note that their shock luminosity is too conservative, partly because the self-similar solution is assumed. Our values of $\rho_{\rm CSM}$ and $v_{\rm sh}$ are larger by a factor of 3 and by a factor of 2, respectively. While they assumed that the CSM extends only up to $R_{\rm CSM} = 10^{15}$ cm, as shown in this work, the CSM should be extended beyond $10^{15}$ cm. Thus, the predicted radio emission should last longer. For $p > 2$, the secondary synchrotron flux in the high-frequency radio band is estimated to be (e.g., Equation (65) of K. Murase 2024)

$$F_\nu^{\rm sync} \approx \frac{(p-2)\epsilon_p L_s}{48\pi(1+Y)d^2} \min[1, f_{pp}] g_{\rm Coul} \left(\frac{\nu}{\nu_b}\right)^{2-\beta_{\rm sync}} \frac{1}{\nu}$$
$$\simeq 350\ \mu{\rm Jy}\ (p-2)\,\epsilon_{p,-1.3}[(1+Y)/9]^{-1} g_{\rm Coul}$$
$$\times \rho^2_{\rm CSM,-16.5} R^3_{15.5} v^{-2}_{\rm sh,9} (\nu/\nu_b)^{2-\beta_{\rm sync}} (100\ {\rm GHz}/\nu), \quad (18)$$

where $L_s$ is the shock kinetic luminosity of the FS and $f_{pp} < 1$ is assumed. Note that $1 - \beta_{\rm syn} = -p/2$ for $\nu > \nu_b$ and $\nu_b \approx \max[\nu_h, \nu_{\rm Coul}]$, and $g_{\rm Coul}$ is the possible correction due to Coulomb losses (K. Murase 2024). Thus, intriguingly, the flux density predicted in the hadronic scenario for $\epsilon_p \sim$ 0.03–0.1 is consistent with the observed NOEMA fluxes at $\delta t \approx$ 23.0 and 38.2 days. We note that the synchrotron spectra of the primary electron emission and secondary electron–positron emission are similar at $\nu > \nu_h (> \nu_{\rm inj})$, where the secondary scenario is effectively compatible with the results of the primary scenario with $\epsilon_e \sim \frac{1}{6}\epsilon_p \min[1, f_{pp}](\gamma_h/\gamma_{\rm inj})^{p-1}$. Also, as indicated in Table 5, Coulomb losses are relevant, especially if the absorption is caused by FFA. For $p = 3$ and $\nu < \nu_{\rm Coul}$, the secondary scenario predicts $F_\nu \propto \nu^0$ while the primary scenario does $F_\nu \propto \nu^{-0.5}$. Apparently, the segment of $F_\nu \propto \nu^0$ seen at $\delta t \approx$ 33 and 57 days is consistent with both primary and secondary scenarios, and more dedicated modeling is necessary to reveal the contribution of proton acceleration in early radio light curves.

## 6. Discussion

### 6.1. SN 2023ixf in the Context of Other Radio/X-Ray Core-collapse Supernovae

We compiled a sample of radio bright CCSNe from the literature in Figure 13 to compare the properties of SN 2023ixf with other CCSNe, particularly SNe IIP. SN 2023ixf occupies the lower luminosity part of the $\nu_{\rm p} - L_{\rm p}$ plot compared to other classes of SNe (Ib/c, IIn). However, it stands out as the brightest among SNe IIP. The dashed lines in the plot represent the mean velocities of the radio emitting shell if the peak flux is determined by SSA (R. A. Chevalier 1998). The inferred velocity of SN 2023ixf is the lowest among other SNe IIP and comparable to SNe IIn, which are known to have very dense CSM. If FFA is the dominant absorption process, the actual velocity will be larger than the ones deduced from this figure, which is indeed the case for SN 2023ixf, as shown in our study.

There are only six SNe IIP with detailed radio follow-up observations; SN 1999em (D. Pooley et al. 2002), SN 2004et (R. A. Chevalier et al. 2006), SN 2004dj (A. J. Nayana et al. 2018), SN 2012aw (N. Yadav et al. 2014), SN 2016X (R. Ruiz-Carmona et al. 2022), and SN 2017eaw (T. Szalai et al. 2019). In Figure 14, we present the 8–10 GHz light curves of these SNe from the literature and compare them with that of SN 2023ixf. The rise time of SN 2023ixf is the slowest among the sample, reaching the peak of the light curve at $\delta t \approx$ 165 days. This indicates a relatively dense CSM for SN 2023ixf compared to other SNe IIP. The mass-loss rates of the literature sample range from $\dot{M} \approx 3 \times 10^{-6}\,M_\odot$ yr$^{-1}$ to

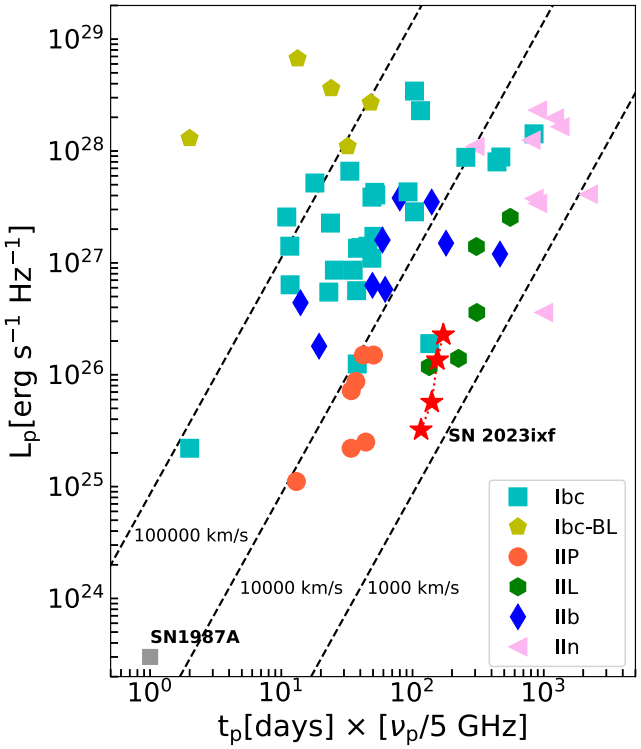


**Figure 13.** Peak radio spectral luminosity of SN 2023ixf (red star symbol) in context of other core-collapse supernovae. SNe Ibc (cyan circles), SNe Ibc-BL (yellow circles), SNe IIP (red circles), SNe IIb (blue circle), and SNe IIn (pink circles). Data are collected from M. F. Bietenholz et al. (2021) and references therein. The dashed line denotes the mean shock velocity in a standard SSA scenario (R. A. Chevalier 1998).

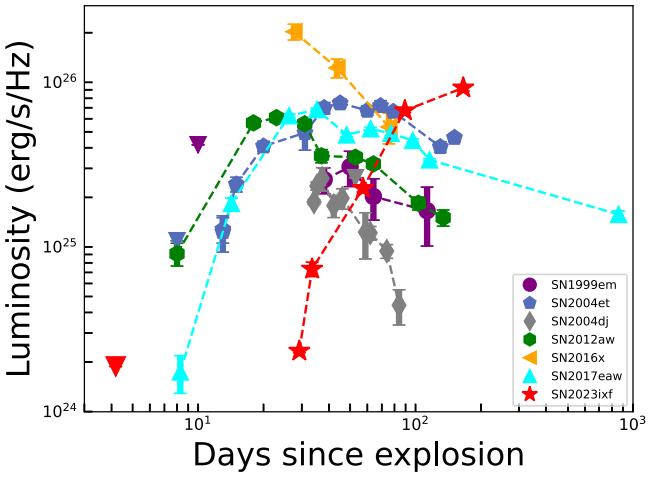


**Figure 14.** Radio light curves (at 8–10 GHz) of SN 2023ixf (red star symbol) in context of other SNe IIP. While the radio luminosity of SN 2023ixf is similar to that of other SNe IIP, the light curve rises significantly later than that of other SNe, indicating denser CSM. References: D. Pooley et al. (2002), R. A. Chevalier et al. (2006), A. J. Nayana et al. (2018), N. Yadav et al. (2014), R. Ruiz-Carmona et al. (2022).

$\dot{M} \approx 2 \times 10^{-5}\, M_\odot\ \mathrm{yr}^{-1}$, whereas the mass-loss rate of SN 2023ixf is $\dot{M} \approx 10^{-4}\, M_\odot\ \mathrm{yr}^{-1}$ for an adopted wind velocity of $v_w = 25\ \mathrm{km\,s}^{-1}$ (a value motivated by the high-resolution spectroscopy study of D. Dickinson et al. 2025, in preparation). We note that the CSM density profile of SN 2023ixf is not entirely $1/r^2$, which implies either a variable wind velocity or mass-loss rate. However, the systematically higher CSM densities of SN 2023ixf suggest that the progenitor of

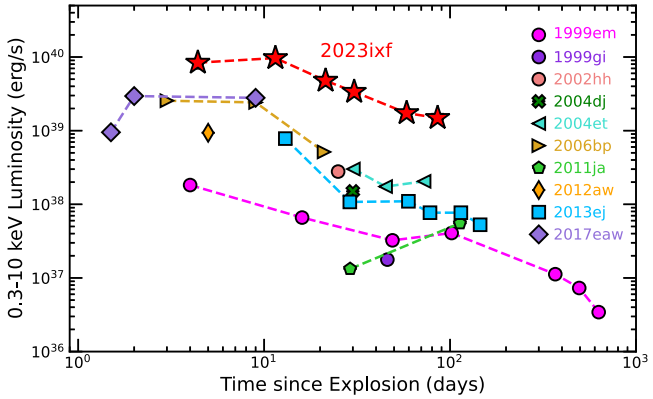


**Figure 15.** Unabsorbed 0.3–10 keV soft X-ray luminosity of the sample of detected Type IIP SNe. SN 2023ixf clearly stands out as the most X-ray-luminous Type IIP SN detected to date. References: E. M. Schlegel (1999, 2001), D. Pooley et al. (2002), D. Pooley & W. H. G. Lewin (2002, 2004), K. Misra et al. (2007), S. Immler et al. (2007), S. Chakraborti et al. (2013, 2016), S. Immler & P. J. Brown (2012), T. Szalai et al. (2019).

SN 2023ixf was experiencing the most extreme mass loss among the SNe IIP progenitors in this sample.

We compiled the X-ray luminosity of all Type IIP SNe detected so far and found that SN 2023ixf is the brightest among them (see Figure 15). Note that we do not plot SN 2016X because it is unclear if the X-ray source faded or not (S. Bose et al. 2019), and the physical association of the X-ray emission with the SN is thus questionable. SN 2023ixf stands out as the most X-ray luminous Type IIP SN found to date and fills the part of the parameter space where X-ray luminous IIP were missing so far (V. V. Dwarkadas 2014).

SN 2023ixf has extreme radio and X-ray properties compared to the sample of known objects. Taken together, the late-time rising radio emission and the significantly luminous X-ray emission of SN 2023ixf imply that the SN shock encountered a medium with properties that are not common among Type IIP SNe.

### 6.2. CSM Density Profile

The main features of the CSM density profile of SN 2023ixf derived from our combined X-ray and radio observations are the following: (1) The CSM densities at shock radii $\approx 3.8 \times 10^{14}$ to $1.4 \times 10^{16}$ cm correspond to $\dot{M} \approx 10^{-4}\, M_\odot \mathrm{yr}^{-1}$ for a stellar wind velocity of $v_w = 25\ \mathrm{km\,s}^{-1}$, which is at least an order of magnitude higher than typical RSG mass-loss rates (N. Smith 2014; E. R. Beasor et al. 2020). (2) The intrinsic X-ray luminosity remains roughly constant for $\delta t < 10$ days and decays as $L_x \propto t^{-1}$ at later epochs, indicating strong interaction with a dense CSM at $r < 10^{15}$ cm. The $\mathrm{NH_{int}}$ declines steeply as $\mathrm{NH_{int}}(t) \propto t^{-2.3}$ at early epochs ($\delta t < 10$ days), and then follows a temporal evolution $\mathrm{NH_{int}}(t) \propto t^{-1}$, consistent with a wind-like CSM. However, the temporal evolution of $\mathrm{NH_{int}}(t)$ inferred from the corresponding EM at $\delta t < 10$ days is significantly discrepant from the observed one and suggests that the neutral column fraction decreases from 70% to 15% between $\delta t \approx 4$ and 11 days. (3) The density profile derived from the X-ray emission measure is wind-like at $R \approx$ (1–7.4) $\times 10^{15}$ cm, and the one from radio SED modeling is flatter ($\rho_{\mathrm{CSM}}(r) \propto r^{-1.3}$) at $R \approx$ (2.9–14) $\times 10^{15}$ cm. If we extrapolate the density profile derived from radio modeling to early X-ray epochs, there is at least an order of magnitude difference in $\rho_{\mathrm{CSM}}(r)$ at $\delta t \approx 4$ days and ~a factor of 5 difference at $\delta t \approx 11$ days (see Figure 8).

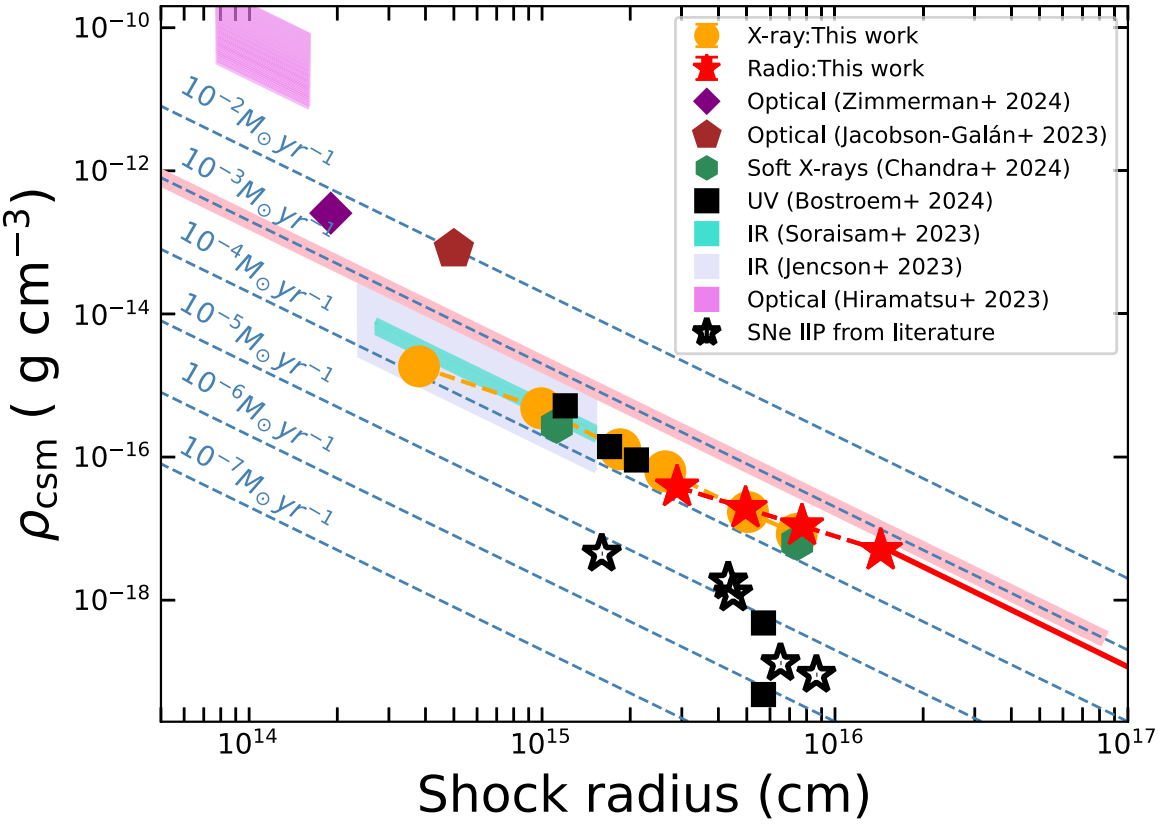


**Figure 16.** Various estimates of CSM densities of SN 2023ixf. The orange circles denote the densities derived from the X-ray emission measure (Section 4.1), and red star symbols mark the densities from radio modeling (Section 5.2) for $\epsilon_e = 10^{-4}$ and $T_e = 5 \times 10^5$ K. The solid red line is the wind-density profile corresponding to the best-fit optical depth in the radio model at $t \approx 165$ days. We also plot density estimates and limits from E. A. Zimmerman et al. (2024), W. V. Jacobson-Galán et al. (2023), P. Chandra et al. (2023b), K. A. Bostroem et al. (2024), M. D. Soraisam et al. (2023), J. E. Jencson et al. (2023), and D. Hiramatsu et al. (2023). The comparison of CSM densities derived from optical analysis with X-ray modeling implies a complex medium (asymmetry and/or clumps) at inner radii ($R < 10^{15}$ cm). The mass-loss rates of other radio bright SNe IIP are marked as black open star symbols: SN 1999em (D. Pooley et al. 2002), SN 2004dj (A. J. Nayana et al. 2018), SN 2004et (R. A. Chevalier et al. 2006), SN 2012aw (N. Yadav et al. 2014), and SN 2016X (R. Ruiz-Carmona et al. 2022). These mass-loss rates are calculated assuming $v_w = 25$ km s$^{-1}$ and $v_{sh} = 10{,}000$ km s$^{-1}$. As a reference, typical mass-loss rates of RSGs are in the range $10^{-6}$–$10^{-5}$ $M_\odot$ yr$^{-1}$ with $v_w = 10$–$50$ km s$^{-1}$ (N. Smith 2014), with a small fraction observed during the short-lived superwind phase, which is characterized by mass-loss rates that are comparable to those of SN 2023ixf $\dot{M} \approx 10^{-4} - 10^{-3}\, M_\odot \mathrm{yr}^{-1}$. The pink line represents the average mass-loss rate of Galactic RSG VY Canis Majoris ($\dot{M} \approx 10^{-3}\, M_\odot \mathrm{yr}^{-1}$) for the last $10^3$ yr inferred from the HST images of the dust scattering nebula around the star (N. Smith 2014).

Various estimates of CSM densities of SN 2023ixf at different distances from the explosion center are reported in the literature (E. Berger et al. 2023; P. Chandra et al. 2023b; B. W. Grefenstette et al. 2023; W. V. Jacobson-Galán et al. 2023; M. D. Soraisam et al. 2023; K. A. Bostroem et al. 2024; J. M. M. Neustadt et al. 2024; E. A. Zimmerman et al. 2024). We compile all these density estimates and place them along with the densities derived from our study in Figure 16 to build a comprehensive picture of the environment of SN 2023ixf.

### 6.2.1. Progenitor in Superwind Phase of Evolution

The typical mass-loss rates of RSGs from empirical studies are $\dot{M} \approx 10^{-6} - 10^{-5}\, M_\odot \mathrm{yr}^{-1}$ (C. de Jager et al. 1988; H. Nieuwenhuijzen & C. de Jager 1990; J. T. van Loon et al. 2005; N. Smith 2014; E. R. Beasor et al. 2020) where the high mass-loss rates (J. T. van Loon et al. 2005) are valid for dust enshrouded RSGs or maser emitters (S. R. Goldman et al. 2017) that are not representative of early phase of RSG evolution. Observations of massive clusters indicate that RSGs with higher mass-loss rates are concentrated toward the end of the RSG phase, where pulsations and turbulence are important, driving them to blueward evolutionary tracks. Some of the most luminous RSGs tend to have higher mass-loss rates, which causes obscuration due to dust. An example of this is the Galactic object VY Canis Majoris, for which the Hubble Space Telescope (HST) images show dust scattering nebula whose density drops sharply at ≈8000 au ($1.2 \times 10^{17}$ cm). The average mass-loss rate of this system is $\dot{M} \approx 10^{-3}\, M_\odot \mathrm{yr}^{-1}$ for the last $10^3$ yr. High mass-loss rates of $\dot{M} \approx (3 - 6) \times 10^{-4}\, M_\odot \mathrm{yr}^{-1}$ are reported for RSG IRC+10420 (G. R. Knapp & M. Morris 1985; R. M. Humphreys et al. 1997) and $\dot{M} \approx 10^{-4} - 10^{-3}\, M_\odot \mathrm{yr}^{-1}$ for NML Cygni (R. Lucas et al. 1992; T. Nagayama et al. 2008). The mass-loss rates derived for SN 2023ixf from X-ray and radio observations are approximately an order of magnitude larger than that of other SNe IIP (see Figure 16) at comparable shock radii. This suggests that the progenitor is likely a very luminous RSG with high mass-loss rates, indicating a "superwind" phase of evolution with vigorous pulsations and turbulence.

Preexplosion archival mid-IR data of the site of SN 2023ixf shows significant variability in the IR light curves with a periodicity of ≈1000 days, indicating pulsational instability (J. E. Jencson et al. 2023; M. D. Soraisam et al. 2023). The initial mass of the progenitor candidate is estimated to be ≈17–20 $M_\odot$ by comparing the luminosity with stellar evolution

models, placing it as one of the most massive progenitors of SNe IIP to date. The progenitor mass-loss rates during 3–19 yr before explosion from SED modeling is $\dot{M} \approx 3 \times 10^{-5} - 3 \times 10^{-4}\, M_{\odot}\ \mathrm{yr}^{-1}$ (J. E. Jencson et al. 2023), and from an empirical period–luminosity based mass-loss prescription is $\dot{M} \approx (2 - 4) \times 10^{-4}\, M_{\odot}\ \mathrm{yr}^{-1}$ (S. R. Goldman et al. 2017; M. D. Soraisam et al. 2023). The mass-loss rates derived from our X-ray and radio analyses correspond to 5–178 yr prior to the explosion and are in line with the values estimated from the preexplosion variability studies.

Shock interactions with the CSM with a mass-loss rate of $\dot{M} \sim (10^{-4} - 10^{-3})\ \ M_{\odot}\ \ \mathrm{yr}^{-1}$ also provide unique opportunities to investigate particle acceleration. High-frequency radio data, especially provided by NOEMA, can be explained by secondary leptons produced by CR protons via inelastic *pp* interactions. Theoretically, not only electrons but also protons should be accelerated, and SNe such as SN 2023ixf can be regarded as the most promising targets for multimessenger observations, especially for nearby events (K. Murase 2018).

#### 6.2.2. Dense Confined CSM

SN 2023ixf exhibits a dense, confined CSM with a mass-loss rate of $\dot{M} \approx 10^{-2}\, M_{\odot}\mathrm{yr}^{-1}$, which drops sharply to $\dot{M} \approx 10^{-4}\, M_{\odot}\ \mathrm{yr}^{-1}$ at $R \approx 10^{15}$ cm (B. W. Grefenstette et al. 2023; W. V. Jacobson-Galán et al. 2023; E. A. Zimmerman et al. 2024). The intrinsic X-ray luminosity stays roughly constant up to $\delta t \approx 10$ days and decays as $L_{\mathrm{x}} \propto t^{-1.1}$, indicating strong interaction with dense CSM at $r < 10^{15}$ cm. While these mass-loss rates are significantly higher than those observed in Galactic RSGs, there is no evidence of IR-bright pre-SN outbursts between 3 and 11 yr ($R \approx 2.4$–$8.7 \times 10^{14}$ cm) before the explosion (J. E. Jencson et al. 2023). IR observations up to ≈10 days before the explosion show no significant changes in colors or fluxes, ruling out the increased activity of the progenitor star in the last 3 yr as the cause of the dense confined CSM (J. E. Jencson et al. 2023). Preexplosion optical imaging studies also provide stringent constraints in this regard, showing no significant activity up to ≈400 days ($R \approx 8.6 \times 10^{13}$ cm) before the explosion (J. M. M. Neustadt et al. 2024). Preexplosion eruptive activity was not detected in the Pan-STARRS light curves spanning 5000d prior explosion to a limiting magnitude of −7 (C. L. Ransome et al. 2024), which is below the brightness of other pre-SN outbursts in the literature. Thus, it is unlikely that the dense CSM around SN 2023ixf is created due to an enhanced pre-SN eruption of the progenitor.

Shock waves launched near the photosphere of an RSG can support a dense region or chromosphere with similar densities that extend up to a few stellar radii. These chromospheric mass models can account for the observational signatures of dense confined CSM, such as flash-ionized emission lines at early times, early light-curve peaks, and extended shock breakout emission, as observed in the case of SN 2023ixf (J. Fuller & D. Tsuna 2024). Therefore, the confined CSM in SN 2023ixf is more likely due to an extended chromosphere rather than an eruptive preexplosion outburst. In the chromospheric model, the shocks are generated by turbulent convection that varies stochastically, possibly resulting in a spatially asymmetric density structure.

Nonthermal emission can also be used as a probe of dense confined CSM because shock acceleration may operate after radiation breaks out from the dense CSM. Radio emission is unlikely to escape while the shock is embedded deep in the dense CSM, and higher-energy particles such as neutrinos and gamma rays provide more promising signatures, as extensively studied for SN 2023ixf (D. Guetta et al. 2023; A. Kheirandish & K. Murase 2023; S. S. Kimura & T. J. Moriya 2024; K. Murase 2024; P. Sarmah 2024; E. Waxman et al. 2025).

#### 6.2.3. Asymmetric and Complex CSM

There are several pieces of evidence suggesting asymmetric CSM in the immediate vicinity ($R < 10^{15}$ cm) of SN 2023ixf from early continuum polarization studies (S. S. Vasylyev et al. 2023; A. Singh et al. 2024) and optical spectral analysis (N. Smith et al. 2023). We tie down these observational signatures from the literature and the results from our analysis to investigate the complexity of the CSM up to distances $R \approx 1.4 \times 10^{16}$ cm from the explosion center.

The CSM densities estimated from optical spectral modeling (W. V. Jacobson-Galán et al. 2023) at $R \approx (0.5$–$1.5) \times 10^{15}$ cm are approximately 2 orders of magnitude higher than the densities derived from our X-ray spectral analysis (see Figure 16), indicating the coexistence of different densities at the same distance from the progenitor. The significantly steep evolution of $\mathrm{NH_{int}}$ ($\mathrm{NH_{int}} \propto t^{-2.3}$) at early times ($\delta t < 10$ days) in contrast to that inferred from the EM also points to arguments on asymmetries and/or clumpiness at $r < 10^{15}$ cm. There is evidence for dense equatorial winds from RSGs, and numerical simulations of an SN interaction with such winds show that a slight variation in the angular density gradient will result in asymmetry in the interaction shell greater than expected from a radial stellar wind (J. M. Blondin et al. 1996). Direct observations of RSGs also provide compelling evidence for asymmetric CSM environments—VY CMa (N. Smith et al. 2009), IRC+10420 (C. Tiffany et al. 2010), and NML Cygni (M. T. Schuster et al. 2009). High-resolution CO spectra of the environment of RSG VY CMa indicate highly asymmetric and clumpy CSM created due to episodic mass loss, possibly connected to pulsational or magnetohydrodynamic activity in the outer layers of the star (N. Smith et al. 2009; R. M. Humphreys et al. 2021). The resulting CSM could be asymmetric at distances up to $R \approx 10^{16}$ cm.

The CSM densities of SN 2023ixf derived from X-ray EM indicate $\rho_{\mathrm{CSM}}(r) \propto r^{-2}$ at $R \approx (1$–$7.4) \times 10^{15}$ cm. Radio spectral modeling implies a density profile $\rho_{\mathrm{CSM}}(r) \propto r^{-1.3}$ at $R \approx (2.9$–$14) \times 10^{15}$ cm. Densities derived in the overlapping region $R \approx (2.9$–$7.4) \times 10^{15}$ cm are consistent with each other for $T_{\mathrm{e}} = 5 \times 10^{5}$ K (see Figure 16). However, if we extrapolate the density profile derived from radio modeling to the early X-ray epoch, there is at least an order of magnitude difference at $t \approx 4$ days and ∼a factor of 5 difference at $t \approx 11$ days. This could imply that the radio and X-ray emissions are coming from two different regions of the CSM. However, the early radio nondetections are consistent with the possible radio emission that could arise from a synchrotron plasma that produces the observed X-ray emission. Thus, there is no strong evidence supporting the coexistence of two density profiles at $R \approx (0.4$–$7.4) \times 10^{15}$ cm. The plausible scenario could be the CSM density profile transitions from $\rho_{\mathrm{CSM}}(r) \propto r^{-2}$ to $r^{-1.3}$ at

$R = (2.9–7.4) \times 10^{15}$ cm. An alternate explanation is the presence of clumpy CSM extending up to the radius probed by the radio observations. The density profile derived from radio modeling assumes a smooth CSM distribution. However, if the CSM is clumpy and has a significant structure such that the filling factor varies with the shock radius (more to less clumpy with radii), the observed radio SEDs can be represented in a wind-like CSM profile.

To summarize, the CSM of SN 2023ixf is highly complex, shaped by the extreme mass loss (effective $\dot{M} \approx 10^{-4}\, M_{\odot}\ \mathrm{yr}^{-1}$) of the progenitor up to around 178 yr before the explosion, leading to asymmetric and clumpy density distribution extending from the immediate environment ($R < 10^{15}$ cm) to distances $R \approx 10^{16}$ cm from the explosion site. Various possible time-dependent mass-loss mechanisms that could create such a density profile include nuclear instabilities, super-Eddington winds, and gravity waves (S. P. Owocki et al. 2004, 2017; W. D. Arnett & C. Meakin 2011; E. Quataert & J. Shiode 2012; N. Smith & W. D. Arnett 2014; E. Quataert et al. 2016; J. Fuller 2017; S. Wu & J. Fuller 2021).

## 7. Conclusions

We carried out extensive X-ray and radio follow-up observations of SN 2023ixf over $\delta t \approx 4$–165 days, covering energy bands 0.3–79 keV in the X-rays and frequency bands 0.7–25 GHz in the radio. We model the spectral and temporal evolution of these observations to investigate the properties of the SN shock and environment. The main findings from our study can be summarized as follows.

1. The X-ray emission is absorbed thermal Bremsstrahlung radiation dominated by the forward shock, where the level of absorption decreases with time. The intrinsic X-ray luminosity remains constant up to $\delta t \approx 10$ days and decays as $L_{\rm x} \propto t^{-1.1}$ at later epochs.
2. The CSM density profile inferred from the X-ray emission measure is wind-like at $R \approx (1–7.4) \times 10^{15}$ cm and deviates from a wind profile at $R < 10^{15}$ cm, as also mirrored by the steep temporal decay of $\mathrm{NH_{int}} \propto t^{-2.3}$ at $\delta t < 10$ days. This can be reconciled by the presence of clumpy CSM in the line of sight at these radii ($R < 10^{15}$ cm).
3. Radio emission is nonthermal synchrotron radiation suppressed by FFA due to CSM of density profile $\rho_{\rm CSM}(r) \propto r^{-1.27}$ at $R \approx (3–14) \times 10^{15}$ cm. The difference in density profiles derived from X-ray and radio analyses could be attributed to a clumpy CSM with a variable filling factor. While various cooling processes could be important depending on the values of shock microphysical parameters ($\epsilon_{\rm e}$ and $\epsilon_{\rm B}$), the dominant FFA determines the CSM density profile and remains agnostic about the intrinsic shape of the SSA spectra. While late-time radio emission may be explained by synchrotron emission from primary electron acceleration, early-time radio fluxes at 84 GHz measured by NOEMA are not consistent with the extrapolated radio SEDs, especially with $p > 2$. We show that this may be an indication of secondary leptons produced by CR protons via *pp* interactions. To model the radio emission accurately, it is essential to systematically account for both primary and secondary components, as well as various cooling losses in the electron energy distribution.
4. The mass-loss rate inferred from X-ray and radio modeling is $\dot{M} \approx 10^{-4} M_{\odot}\ \mathrm{yr}^{-1}$ for a stellar wind velocity of $v_{\rm w} = 25\ \mathrm{km\ s^{-1}}$ during ≈3–178 yr preceding the core collapse. This rate is about an order of magnitude higher than those derived for other radio/X-ray bright SNe IIP in the literature and significantly exceeds the typical mass-loss rates of RSGs. This places the progenitor of SN 2023ixf among those with the most extreme mass-loss rates.

Our extensive multiwavelength observations and modeling of SN 2023ixf paint a picture of extremely complex CSM with asymmetries and clumps from the immediate environment to $\approx 10^{16}$ cm from the explosion center. While various time-dependent mass-loss mechanisms can create such an intricate environment, our study demonstrates the need for detailed high-cadence follow-up observations using optical, X-ray, and radio facilities to fully map such a complex CSM structure.

## Acknowledgments

This work is based on observations carried out under project No. d23ab with the IRAM NOEMA Interferometer [30 m telescope]. IRAM is supported by INSU/CNRS (France), MPG (Germany), and IGN (Spain). The National Radio Astronomy Observatory is a facility of the National Science Foundation operated under cooperative agreement by Associated Universities, Inc. We thank the staff of the GMRT that made these observations possible. The GMRT is run by the National Centre for Radio Astrophysics of the Tata Institute of Fundamental Research. This research has made use of the NuSTAR Data Analysis Software (NuSTARDAS) jointly developed by the ASI Space Science Data Center (SSDC, Italy) and the California Institute of Technology (Caltech, USA). Partially based on observations obtained with XMM-Newton, an ESA science mission with instruments and contributions directly funded by ESA Member States and NASA. This paper employs a list of Chandra data sets, obtained by the Chandra X-ray Observatory, contained in doi:10.25574/cdc.351. This research has made use of the XRT Data Analysis Software (XRTDAS) developed under the responsibility of the ASI Science Data Center (ASDC), Italy. This work made use of data supplied by the UK Swift Science Data Centre at the University of Leicester. This research has made use of data and software provided by the High Energy Astrophysics Science Archive Research Center (HEASARC), which is a service of the Astrophysics Science Division at NASA/GSFC.

This work was performed in part at the Aspen Center for Physics, which is supported by National Science Foundation grant PHY-2210452. The collaboration of D.T. and R.M. was facilitated by interactions that were funded by the Gordon and Betty Moore Foundation through grant GBMF5076. R.M. acknowledges support by the National Science Foundation under award No. AST-2221789 and AST-2224255, and by NASA under grant 80NSSC22K1587. The TReX team at UC Berkeley is partially funded by the Heising-Simons Foundation under grant 2021-3248 (PI: Margutti). The work of K.M. is partially supported by the NSF grants No. AST-2108466, No. AST-2108467, and No. AST-2308021, and KAKENHI No.

20H05852. D.T. acknowledges support by the Sherman Fairchild Postdoctoral Fellowship at the California Institute of Technology. P.C. acknowledges support from NASA through Chandra award No. DD3-24141X issued by the Chandra X-ray Center. K.M. acknowledges support from the Japan Society for the Promotion of Science (JSPS) KAKENHI grant JP24KK0070 and 24H01810. F.D.C. acknowledges support from DGAPA/PAPIIT grant IN113424. Andrea Reguitti acknowledges financial support from the GRAWITA Large Program grant (PI P. D'Avanzo) and the PRIN-INAF 2022 "Shedding light on the nature of gap transients: from the observations to the models". G.M. acknowledges financial support from the INAF mini-grant "The high-energy view of jets and transients" (Bando Ricerca Fondamentale INAF 2022). S.C. thanks Norbert Schartel for granting the first XMM-Newton observation. S.C. acknowledges support from ASI. B.M. acknowledges financial support from the State Agency for Research of the Spanish Ministry of Science and Innovation, and FEDER, UE, under grant PID2022-136828NB-C41/MICIU/AEI/10.13039/501100011033, and through the Unit of Excellence Marìa de Maeztu 2020–2023 award to the Institute of Cosmos Sciences (CEX2019- 000918-M). The European Research Council (ERC) under the European Union's Horizon 2020 research and innovation program ('EuroFlash': grant agreement No. 101098079).

*Facilities:* HST (STIS), Swift (XRT and UVOT), AAVSO, CTIO:1.3m, CTIO:1.5m, CXO.

*Software:* astropy (Astropy Collaboration et al. 2013, 2018).

## Appendix A
## Radio Data Table

Tables 6, 7, and 8 show radio observation logs and flux measurements of SN 2023ixf with NOEMA, VLA, and GMRT, respectively.

**Table 6**
NOEMA Observations of SN 2023ixf

| Start Date (dd/mm/yy) | Project ID | Centroid MJD | Phase[a] (days) | Frequency (GHz) | Flux Density[b] ($\mu$Jy) |
|---|---|---|---|---|---|
| 10/06/2023 | d23ab | 60105.83 | 23.09 | 84 | 212 ± 55 |
| 26/06/2023 | d23ab | 60121.04 | 38.30 | 84 | 359 ± 62 |
| 19/07/2023 | d23ab | 60144.87 | 62.13 | 84 | 206 ± 64 |
| 09/06/2023 | d23ab | 60104.11 | 21.37 | 144 | <200 |
| 26/06/2023 | d23ab | 60121.94 | 39.20 | 144 | <200 |
| 18/07/2023 | d23ab | 60143.93 | 61.19 | 144 | <365 |

**Notes.**
[a] With respect to explosion.
[b] The uncertainties on flux measurements are $1\sigma$, and upper limits are $5\sigma$.

**Table 7**
VLA Observations of SN 2023ixf

| Start Date (dd/mm/yy) | Project ID | VLA Config. | Centroid MJD | Phase[a] (days) | Frequency (GHz) | Bandwidth (GHz) | Flux Density[b] ($\mu$Jy) |
|---|---|---|---|---|---|---|---|
| 23/05/2023 | SF151070 | B | 60087.01 | 4.18 | 10 | 2.0 | <33 $\mu$Jy |
| 17/06/2023 | SF151070 | A | 60112.04 | 29.21 | 10 | 2.0 | 41 ± 8 $\mu$Jy |
| 21/06/2023 | SF151070 | A | 60116.30 | 33.45 | 8.5 | 0.5 | 51 ± 12 |
| 21/06/2023 | SF151070 | A | 60116.30 | 33.45 | 9.5 | 0.5 | 109 ± 11 |
| 21/06/2023 | SF151070 | A | 60116.30 | 33.45 | 10.5 | 0.5 | 129 ± 15 |
| 21/06/2023 | SF151070 | A | 60116.30 | 33.45 | 11.5 | 0.5 | 134 ± 16 |
| 21/06/2023 | SF151070 | A | 60116.30 | 33.45 | 12.5 | 0.5 | 154 ± 14 |
| 21/06/2023 | SF151070 | A | 60116.30 | 33.45 | 13.5 | 0.5 | 198 ± 17 |
| 21/06/2023 | SF151070 | A | 60116.30 | 33.45 | 14.5 | 0.5 | 211 ± 18 |
| 21/06/2023 | SF151070 | A | 60116.30 | 33.45 | 15.5 | 0.5 | 229 ± 19 |
| 21/06/2023 | SF151070 | A | 60116.30 | 33.45 | 16.5 | 0.5 | 267 ± 21 |
| 21/06/2023 | SF151070 | A | 60116.30 | 33.45 | 17.5 | 0.5 | 304 ± 23 |
| 21/06/2023 | SF151070 | A | 60116.30 | 33.45 | 18.5 | 0.5 | 316 ± 23 |
| 21/06/2023 | SF151070 | A | 60116.30 | 33.45 | 19.5 | 0.5 | 330 ± 23 |
| 21/06/2023 | SF151070 | A | 60116.30 | 33.45 | 20.5 | 0.5 | 293 ± 24 |
| 21/06/2023 | SF151070 | A | 60116.30 | 33.45 | 21.5 | 0.5 | 290 ± 29 |
| 21/06/2023 | SF151070 | A | 60116.30 | 33.45 | 22.5 | 0.5 | 333 ± 31 |
| 21/06/2023 | SF151070 | A | 60116.30 | 33.45 | 23.5 | 0.5 | 310 ± 29 |
| 21/06/2023 | SF151070 | A | 60116.30 | 33.45 | 24.5 | 0.5 | 334 ± 26 |
| 21/06/2023 | SF151070 | A | 60116.30 | 33.45 | 25.5 | 0.5 | 287 ± 29 |

**Table 7**
(Continued)

| Start Date (dd/mm/yy) | Project ID | VLA Config. | Centroid MJD | Phase[a] (days) | Frequency (GHz) | Bandwidth (GHz) | Flux Density[b] ($\mu$Jy) |
|---|---|---|---|---|---|---|---|
| 15/07/2023 | SF151070 | A | 60140.14 | 57.31 | 2.5 | 0.5 | <45 |
| 15/07/2023 | SF151070 | A | 60140.14 | 57.31 | 3.5 | 0.5 | <45 |
| 15/07/2023 | SF151070 | A | 60140.14 | 57.31 | 4.5 | 0.5 | 82 ± 14 |
| 15/07/2023 | SF151070 | A | 60140.14 | 57.31 | 5.5 | 0.5 | 131 ± 20 |
| 15/07/2023 | SF151070 | A | 60140.14 | 57.31 | 6.5 | 0.5 | 192 ± 21 |
| 15/07/2023 | SF151070 | A | 60140.14 | 57.31 | 7.5 | 0.5 | 269 ± 17 |
| 15/07/2023 | SF151070 | A | 60140.14 | 57.31 | 8.5 | 0.5 | 345 ± 12 |
| 15/07/2023 | SF151070 | A | 60140.14 | 57.31 | 9.5 | 0.5 | 393 ± 21 |
| 15/07/2023 | SF151070 | A | 60140.14 | 57.31 | 10.5 | 0.5 | 399 ± 28 |
| 15/07/2023 | SF151070 | A | 60140.14 | 57.31 | 11.5 | 0.5 | 439 ± 28 |
| 15/07/2023 | SF151070 | A | 60140.14 | 57.31 | 12.5 | 0.5 | 517 ± 31 |
| 15/07/2023 | SF151070 | A | 60140.14 | 57.31 | 13.5 | 0.5 | 550 ± 32 |
| 15/07/2023 | SF151070 | A | 60140.14 | 57.31 | 14.5 | 0.5 | 517 ± 30 |
| 15/07/2023 | SF151070 | A | 60140.14 | 57.31 | 15.5 | 0.5 | 549 ± 35 |
| 15/07/2023 | SF151070 | A | 60140.14 | 57.31 | 16.5 | 0.5 | 530 ± 30 |
| 15/07/2023 | SF151070 | A | 60140.14 | 57.31 | 17.5 | 0.5 | 549 ± 37 |
| 15/07/2023 | SF151070 | A | 60140.14 | 57.31 | 18.5 | 0.5 | 515 ± 28 |
| 15/07/2023 | SF151070 | A | 60140.14 | 57.31 | 19.5 | 0.5 | 539 ± 37 |
| 15/07/2023 | SF151070 | A | 60140.14 | 57.31 | 20.5 | 0.5 | 545 ± 40 |
| 15/07/2023 | SF151070 | A | 60140.14 | 57.31 | 21.5 | 0.5 | 481 ± 50 |
| 15/07/2023 | SF151070 | A | 60140.14 | 57.31 | 22.5 | 0.5 | 442 ± 37 |
| 15/07/2023 | SF151070 | A | 60140.14 | 57.31 | 23.5 | 0.5 | 457 ± 43 |
| 15/07/2023 | SF151070 | A | 60140.14 | 57.31 | 24.5 | 0.5 | 442 ± 35 |
| 15/07/2023 | SF151070 | A | 60140.14 | 57.31 | 25.5 | 0.5 | 402 ± 31 |
| 16/08/2023 | SF151070 | A | 60172.13 | 89.30 | 2.5 | 0.5 | <45 |
| 16/08/2023 | SF151070 | A | 60172.13 | 89.30 | 3.5 | 0.5 | 125 ± 16 |
| 16/08/2023 | SF151070 | A | 60172.13 | 89.30 | 4.5 | 0.5 | 338 ± 25 |
| 16/08/2023 | SF151070 | A | 60172.13 | 89.30 | 5.5 | 0.5 | 645 ± 39 |
| 16/08/2023 | SF151070 | A | 60172.13 | 89.30 | 6.5 | 0.5 | 854 ± 47 |
| 16/08/2023 | SF151070 | A | 60172.13 | 89.30 | 7.5 | 0.5 | 1023 ± 55 |
| 16/08/2023 | SF151070 | A | 60172.13 | 89.30 | 8.5 | 0.5 | 1182 ± 60 |
| 16/08/2023 | SF151070 | A | 60172.13 | 89.30 | 9.5 | 0.5 | 1236 ± 66 |
| 16/08/2023 | SF151070 | A | 60172.13 | 89.30 | 10.5 | 0.5 | 1183 ± 68 |
| 16/08/2023 | SF151070 | A | 60172.13 | 89.30 | 11.5 | 0.5 | 1259 ± 79 |
| 16/08/2023 | SF151070 | A | 60172.13 | 89.30 | 12.5 | 0.5 | 1337 ± 71 |
| 16/08/2023 | SF151070 | A | 60172.13 | 89.30 | 13.5 | 0.5 | 1190 ± 65 |
| 16/08/2023 | SF151070 | A | 60172.13 | 89.30 | 14.5 | 0.5 | 1251 ± 68 |
| 16/08/2023 | SF151070 | A | 60172.13 | 89.30 | 15.5 | 0.5 | 1193 ± 64 |
| 16/08/2023 | SF151070 | A | 60172.13 | 89.30 | 16.5 | 0.5 | 1111 ± 61 |
| 16/08/2023 | SF151070 | A | 60172.13 | 89.30 | 17.5 | 0.5 | 1110 ± 63 |
| 16/08/2023 | SF151070 | A | 60172.13 | 89.30 | 18.5 | 0.5 | 1068 ± 65 |
| 16/08/2023 | SF151070 | A | 60172.13 | 89.30 | 19.5 | 0.5 | 1052 ± 62 |
| 16/08/2023 | SF151070 | A | 60172.13 | 89.30 | 20.5 | 0.5 | 1041 ± 61 |
| 16/08/2023 | SF151070 | A | 60172.13 | 89.30 | 21.5 | 0.5 | 1068 ± 65 |
| 16/08/2023 | SF151070 | A | 60172.13 | 89.30 | 22.5 | 0.5 | 1023 ± 77 |
| 16/08/2023 | SF151070 | A | 60172.13 | 89.30 | 23.5 | 0.5 | 876 ± 60 |
| 16/08/2023 | SF151070 | A | 60172.13 | 89.30 | 24.5 | 0.5 | 784 ± 56 |
| 16/08/2023 | SF151070 | A | 60172.13 | 89.30 | 25.5 | 0.5 | 695 ± 59 |
| 31/10/2023 | SF151070 | D | 60248.61 | 165.78 | 2.5 | 0.5 | <4593 |
| 31/10/2023 | SF151070 | D | 60248.61 | 165.78 | 3.5 | 0.5 | <4393 |
| 31/10/2023 | SF151070 | D | 60248.61 | 165.78 | 04.5 | 0.5 | 2032 ± 170 |
| 31/10/2023 | SF151070 | D | 60248.61 | 165.78 | 05.5 | 0.5 | 2155 ± 146 |
| 31/10/2023 | SF151070 | D | 60248.61 | 165.78 | 06.5 | 0.5 | 2111 ± 157 |
| 31/10/2023 | SF151070 | D | 60248.61 | 165.78 | 07.5 | 0.5 | 2060 ± 137 |
| 31/10/2023 | SF151070 | D | 60248.61 | 165.78 | 08.5 | 0.5 | 1923 ± 124 |
| 31/10/2023 | SF151070 | D | 60248.61 | 165.78 | 09.5 | 0.5 | 1826 ± 119 |
| 31/10/2023 | SF151070 | D | 60248.61 | 165.78 | 10.5 | 0.5 | 1627 ± 109 |
| 31/10/2023 | SF151070 | D | 60248.61 | 165.78 | 11.5 | 0.5 | 1605 ± 107 |
| 31/10/2023 | SF151070 | D | 60248.61 | 165.78 | 12.5 | 0.5 | 1599 ± 122 |

**Table 7**
(Continued)

| Start Date (dd/mm/yy) | Project ID | VLA Config. | Centroid MJD | Phase[a] (days) | Frequency (GHz) | Bandwidth (GHz) | Flux Density[b] ($\mu$Jy) |
|---|---|---|---|---|---|---|---|
| 31/10/2023 | SF151070 | D | 60248.61 | 165.78 | 13.5 | 0.5 | 1549 ± 102 |
| 31/10/2023 | SF151070 | D | 60248.61 | 165.78 | 14.5 | 0.5 | 1402 ± 116 |
| 31/10/2023 | SF151070 | D | 60248.61 | 165.78 | 15.5 | 0.5 | 1367 ± 98 |
| 31/10/2023 | SF151070 | D | 60248.61 | 165.78 | 16.5 | 0.5 | 1368 ± 98 |
| 31/10/2023 | SF151070 | D | 60248.61 | 165.78 | 17.5 | 0.5 | 1279 ± 75 |

**Notes.**
[a] With respect to explosion.
[b] The uncertainties on flux measurements include map rms values ($1\sigma$) and a 5% systematic uncertainty on the flux density added in quadrature. The flux density upper limits are $3\sigma$.

**Table 8**
GMRT Observations of SN 2023ixf

| Start Date (dd/mm/yy) | Project ID | Centroid MJD | Phase[a] (days) | Frequency (GHz) | Bandwidth (GHz) | Flux Density[b] ($\mu$Jy) |
|---|---|---|---|---|---|---|
| 22/05/2023 | 44_095 | 60086.00 | 3.17 | 1.25 | 0.28 | <75 |
| 22/05/2023 | 44_095 | 60086.00 | 3.17 | 0.75 | 0.20 | <200 |
| 28/05/2023 | 44_095 | 60092.00 | 9.17 | 1.25 | 0.28 | <80 |
| 31/05/2023 | 44_095 | 60095.00 | 12.17 | 0.75 | 0.20 | <200 |
| 02/07/2023 | 44_095 | 60127.00 | 44.17 | 1.25 | 0.28 | <68 |
| 29/07/2023 | 44_095 | 60154.00 | 71.17 | 1.25 | 0.28 | <200 |
| 29/07/2023 | 44_095 | 60154.00 | 71.17 | 0.75 | 0.20 | <75 |
| 07/09/2023 | 44_095 | 60194.00 | 111.17 | 0.75 | 0.20 | <200 |
| 08/09/2023 | 44_095 | 60195.30 | 112.47 | 1.25 | 0.28 | <70 |
| 31/10/2023 | 45_091 | 60248.00 | 165.17 | 1.25 | 0.28 | 148 ± 31 |

**Notes.**
[a] With respect to explosion.
[b] The uncertainties on flux measurements are $1\sigma$, and upper limits are $3\sigma$.

## Appendix B
## X-Ray Observation Logs

Table 9 shows the details of X-ray observations of SN 2023ixf with XMM-Newton, CXO, and NuSTAR.

**Table 9**
X-Ray Observations of SN 2023ixf with XMM-Newton, CXO, and NuSTAR

| Instrument | Start Date (dd/mm/yy) | Mid Time[a] (days) | Obs ID | Exposure Time[b] (ks) | PI |
|---|---|---|---|---|---|
| NuSTAR | 2023-05-22 | 4.38 | 90902520002 | 42.2/42.0 | B. Grefenstette |
| XMM/EPIC-pn | 2023-05-27 | 9.01 | 0931790101[c] | 62.8 | S. Campana |
| XMM/EPIC-MOS1 | 2023-05-27 | 9.01 | 0931790101[c] | 69.9 | S. Campana |
| XMM/EPIC-MOS2 | 2023-05-27 | 9.01 | 0931790101[c] | 70.0 | S. Campana |
| NuSTAR | 2023-05-29 | 11.46 | 90902520004 | 42.0/41.6 | B. Grefenstette |
| CXO | 2023-05-31 | 12.95 | 27862 | 20.1 | P. Chandra |
| NuSTAR | 2023-06-08 | 21.44 | 90902520006 | 63.4/62.7 | B. Grefenstette |
| NuSTAR | 2023-06-17 | 30.51 | 80902505002 | 56.1/55.6 | R. Margutti |
| XMM/EPIC-pn | 2023-06-18 | 30.79 | 0921180101[d] | 10.0 | R. Margutti |
| XMM/EPIC-MOS1 | 2023-06-18 | 30.79 | 0921180101[d] | 11.8 | R. Margutti |
| XMM/EPIC-MOS2 | 2023-06-18 | 30.79 | 0921180101[d] | 11.8 | R. Margutti |
| XMM/EPIC-pn | 2023-07-15 | 58.16 | 0921180301[d] | 13.4 | R. Margutti |
| XMM/EPIC-MOS1 | 2023-07-15 | 58.16 | 0921180301[d] | 18.4 | R. Margutti |
| XMM/EPIC-MOS2 | 2023-07-15 | 58.16 | 0921180301[d] | 18.7 | R. Margutti |
| NuSTAR | 2023-07-15 | 58.43 | 80902505004 | 53.3/52.8 | R. Margutti |
| CXO | 2023-08-11 | 84.93 | 27862 | 10.5 | P. Chandra |
| CXO | 2023-08-12 | 85.67 | 28374 | 9.9 | P. Chandra |

**Notes.**
[a] With respect to explosion.
[b] After excluding intervals of time with large background (e.g., due to proton flaring). For NuSTAR, we report the exposure times for module A and module B.
[c] Observations acquired with the thick filter.
[d] Observations acquired with the medium filter.

## ORCID iDs

Nayana A. J. https://orcid.org/0000-0002-8070-5400
Raffaella Margutti https://orcid.org/0000-0003-4768-7586
Eli Wiston https://orcid.org/0009-0002-4843-2913
Ryan Chornock https://orcid.org/0000-0002-7706-5668
Sergio Campana https://orcid.org/0000-0001-6278-1576
Tanmoy Laskar https://orcid.org/0000-0003-1792-2338
Kohta Murase https://orcid.org/0000-0002-5358-5642
Melanie Krips https://orcid.org/0000-0001-6971-4851
Giulia Migliori https://orcid.org/0000-0003-0216-8053
Daichi Tsuna https://orcid.org/0000-0002-6347-3089
Kate D. Alexander https://orcid.org/0000-0002-8297-2473
Poonam Chandra https://orcid.org/0000-0002-0844-6563
Michael Bietenholz https://orcid.org/0000-0002-0592-4152
Edo Berger https://orcid.org/0000-0002-9392-9681
Roger A. Chevalier https://orcid.org/0000-0002-9117-7244
Fabio De Colle https://orcid.org/0000-0002-3137-4633
Luc Dessart https://orcid.org/0000-0003-0599-8407
Rebecca Diesing https://orcid.org/0000-0002-6679-0012
Brian W. Grefenstette https://orcid.org/0000-0002-1984-2932
Wynn V. Jacobson-Galán https://orcid.org/0000-0003-1103-3409
Keiichi Maeda https://orcid.org/0000-0003-2611-7269
Benito Marcote https://orcid.org/0000-0001-9814-2354
Daisy Matthews https://orcid.org/0000-0002-4513-3849
Dan Milisavljevic https://orcid.org/0000-0002-0763-3885
Alak K. Ray https://orcid.org/0000-0003-2404-0018
Andrea Reguitti https://orcid.org/0000-0003-4254-2724
Ava Polzin https://orcid.org/0000-0002-5283-933X

## References

Anders, E., & Grevesse, N. 1989, GeCoA, 53, 197
Arnett, W. D., & Meakin, C. 2011, ApJ, 741, 33
Asplund, M., Grevesse, N., Sauval, A. J., & Scott, P. 2009, ARA&A, 47, 481
Astropy Collaboration, Price-Whelan, A. M., Sipőcz, B. M., et al. 2018, AJ, 156, 123
Astropy Collaboration, Robitaille, T. P., Tollerud, E. J., et al. 2013, A&A, 558, A33
Beasor, E. R., Davies, B., Smith, N., et al. 2020, MNRAS, 492, 5994
Berger, E., Keating, G. K., Margutti, R., et al. 2023, ApJL, 951, L31
Bietenholz, M. F., Bartel, N., Argo, M., et al. 2021, ApJ, 908, 75
Björnsson, C.-I., & Fransson, C. 2004, ApJ, 605, 823
Blondin, J. M., Lundqvist, P., & Chevalier, R. A. 1996, ApJ, 472, 257
Boian, I., & Groh, J. H. 2020, MNRAS, 496, 1325
Bose, S., Dong, S., Elias-Rosa, N., et al. 2019, ApJL, 873, L3
Bostroem, K. A., Pearson, J., Shrestha, M., et al. 2023, ApJL, 956, L5
Bostroem, K. A., Sand, D. J., Dessart, L., et al. 2024, ApJL, 973, L47
Brethauer, D., Margutti, R., Milisavljevic, D., et al. 2022, ApJ, 939, 105
Bruch, R. J., Gal-Yam, A., Schulze, S., et al. 2021, ApJ, 912, 46
Bruch, R. J., Gal-Yam, A., Yaron, O., et al. 2023, ApJ, 952, 119
Burrows, D. N., Hill, J. E., Nousek, J. A., et al. 2005, SSRv, 120, 165
Caprioli, D. 2023, arXiv:2307.00284
CASA Team, Bean, B., Bhatnagar, S., et al. 2022, PASP, 134, 114501
Chakraborti, S., Ray, A., Smith, R., et al. 2013, ApJ, 774, 30
Chakraborti, S., Ray, A., Smith, R., et al. 2016, ApJ, 817, 22
Chakraborti, S., Yadav, N., Ray, A., et al. 2012, ApJ, 761, 100
Chandra, P., Chevalier, R. A., Chugai, N., et al. 2012, ApJ, 755, 110
Chandra, P., Chevalier, R. A., Maeda, K., Ray, A. K., & Nayana, A. J. 2024, ApJL, 963, L4

Chandra, P., Chevalier, R., Nayana, A. J., Maeda, K., & Ray, A. 2023a, ATel, 16052, 1
Chevalier, R. A. 1982, ApJ, 258, 790
Chevalier, R. A. 1998, ApJ, 499, 810
Chevalier, R. A., & Fransson, C. 1985, in Supernovae as Distance Indicators, ed. N. Bartel, 224 (Berlin: Springer), 123
Chevalier, R. A., & Fransson, C. 2017, in Handbook of Supernovae, ed. A. W. Alsabti & P. Murdin (Berlin: Springer), 875
Chevalier, R. A., Fransson, C., & Nymark, T. K. 2006, ApJ, 641, 1029
Das, S., & Ray, A. 2017, ApJ, 851, 138
de Jager, C., Nieuwenhuijzen, H., & van der Hucht, K. A. 1988, A&AS, 72, 259
Diesing, R., & Caprioli, D. 2019, PhRvL, 123, 071101
Diesing, R., & Caprioli, D. 2021, ApJ, 922, 1
Dwarkadas, V. V. 2014, MNRAS, 440, 1917
Dwarkadas, V. V., Dewey, D., & Bauer, F. 2010, MNRAS, 407, 812
Evans, P. A., Beardmore, A. P., Page, K. L., et al. 2009, MNRAS, 397, 1177
Foreman-Mackey, D., Hogg, D. W., Lang, D., & Goodman, J. 2013, PASP, 125, 306
Förster, F., Moriya, T. J., Maureira, J. C., et al. 2018, NatAs, 2, 808
Fransson, C. 1984, A&A, 133, 264
Fransson, C., & Björnsson, C.-I. 1998, ApJ, 509, 861
Fransson, C., Lundqvist, P., & Chevalier, R. A. 1996, ApJ, 461, 993
Fuller, J. 2017, MNRAS, 470, 1642
Fuller, J., & Tsuna, D. 2024, OJAp, 7, 47
Gehrels, N., Chincarini, G., Giommi, P., et al. 2004, ApJ, 611, 1005
Goldman, S. R., van Loon, J. T., Zijlstra, A. A., et al. 2017, MNRAS, 465, 403
Grefenstette, B. W., Brightman, M., Earnshaw, H. P., Harrison, F. A., & Margutti, R. 2023, ApJL, 952, L3
Greisen, E. W. 2003, in Information Handling in Astronomy—Historical Vistas, ed. A. Heck (Dordrecht: Kluwer), 109
Guetta, D., Langella, A., Gagliardini, S., & Della Valle, M. 2023, ApJL, 955, L9
Gupta, S., Caprioli, D., & Spitkovsky, A. 2024, ApJ, 976, 10
HI4PI Collaboration, Ben Bekhti, N., Flöer, L., et al. 2016, A&A, 594, A116
Hiramatsu, D., Tsuna, D., Berger, E., et al. 2023, ApJL, 955, L8
Hosseinzadeh, G., Farah, J., Shrestha, M., et al. 2023, ApJL, 953, L16
Houck, J. C., Bregman, J. N., Chevalier, R. A., & Tomisaka, K. 1998, ApJ, 493, 431
Humphreys, R. M., Davidson, K., Richards, A. M. S., et al. 2021, AJ, 161, 98
Humphreys, R. M., Smith, N., Davidson, K., et al. 1997, AJ, 114, 2778
Immler, S., & Brown, P. J. 2012, ATel, 3995, 1
Immler, S., Brown, P. J., Milne, P., et al. 2007, ApJ, 664, 435
Jacobson-Galán, W. V., Davis, K. W., Kilpatrick, C. D., et al. 2024a, ApJ, 972, 177
Jacobson-Galán, W. V., Dessart, L., Davis, K. W., et al. 2024b, ApJ, 970, 189
Jacobson-Galán, W. V., Dessart, L., Jones, D. O., et al. 2022, ApJ, 924, 15
Jacobson-Galán, W. V., Dessart, L., Margutti, R., et al. 2023, ApJL, 954, L42
Jencson, J. E., Pearson, J., Beasor, E. R., et al. 2023, ApJL, 952, L30
Katz, B., Sapir, N., & Waxman, E. 2012, in IAU Symp. 279, Death of Massive Stars: Supernovae and Gamma-Ray Bursts, ed. P. Roming, N. Kawai, & E. Pian (Cambridge: Cambridge Univ. Press), 274
Khazov, D., Yaron, O., Gal-Yam, A., et al. 2016, ApJ, 818, 3
Kheirandish, A., & Murase, K. 2023, ApJL, 956, L8
Kilpatrick, C. D., & Foley, R. J. 2018, MNRAS, 481, 2536
Kilpatrick, C. D., Foley, R. J., Jacobson-Galán, W. V., et al. 2023, ApJL, 952, L23
Kimura, S. S., & Moriya, T. J. 2024, arXiv:2409.18935
Knapp, G. R., & Morris, M. 1985, ApJ, 292, 640
Kohmura, Y., Inoue, H., Aoki, T., et al. 1994, PASJ, 46, L157
Leonard, D. C., Filippenko, A. V., Barth, A. J., & Matheson, T. 2000, ApJ, 536, 239
Lucas, R., Bujarrabal, V., Guilloteau, S., et al. 1992, A&A, 262, 491
Lundqvist, P., & Fransson, C. 1991, ApJ, 380, 575
Mao, Y., Zhang, M., Cai, G., et al. 2023, TNSAN, 130, 1
Margutti, R., Kamble, A., Milisavljevic, D., et al. 2017, ApJ, 835, 140
Margutti, R., Soderberg, A. M., Chomiuk, L., et al. 2012, ApJ, 751, 134
Margutti, R., Zaninoni, E., Bernardini, M. G., et al. 2013, MNRAS, 428, 729
Matthews, D., Margutti, R., AJ, N., et al. 2023a, ATel, 16091, 1
Matthews, D., Margutti, R., Alexander, K. D., et al. 2023b, ATel, 16056, 1
Matzner, C. D., & McKee, C. F. 1999, ApJ, 510, 379
McMullin, J. P., Waters, B., Schiebel, D., Young, W., & Golap, K. 2007, in ASP Conf. Ser. 376, Astronomical Data Analysis Software and Systems XVI, ed. R. A. Shaw, F. Hill, & D. J. Bell (San Francisco, CA: ASP), 127
Mereminskiy, I. A., Lutovinov, A. A., Sazonov, S. Y., et al. 2023, ATel, 16065, 1
Misra, K., Pooley, D., Chandra, P., et al. 2007, MNRAS, 381, 280
Murase, K. 2018, PhRvD, 97, 081301
Murase, K. 2024, PhRvD, 109, 103020
Murase, K., Thompson, T. A., Lacki, B. C., & Beacom, J. F. 2011, PhRvD, 84, 043003
Murase, K., Thompson, T. A., & Ofek, E. O. 2014, MNRAS, 440, 2528
Nagayama, T., Takeda, K., Omodaka, T., et al. 2008, PASJ, 60, 1069
Nayana, A. J., Chandra, P., & Ray, A. K. 2018, ApJ, 863, 163
Nayana, A. J., Chandra, P., Roy, S., et al. 2017, MNRAS, 467, 155
Neustadt, J. M. M., Kochanek, C. S., & Smith, M. R. 2024, MNRAS, 527, 5366
Nieuwenhuijzen, H., & de Jager, C. 1990, A&A, 231, 134
Niu, Z., Sun, N.-C., Maund, J. R., et al. 2023, ApJL, 955, L15
Nymark, T. K., Fransson, C., & Kozma, C. 2006, A&A, 449, 171
Offringa, A. R., & Smirnov, O. 2017, MNRAS, 471, 301
Owocki, S. P., Gayley, K. G., & Shaviv, N. J. 2004, ApJ, 616, 525
Owocki, S. P., Townsend, R. H. D., & Quataert, E. 2017, MNRAS, 472, 3749
Panjkov, S., Auchettl, K., Shappee, B. J., et al. 2023, PASA, 41, e059
Park, J., Caprioli, D., & Spitkovsky, A. 2015, PhRvL, 114, 085003
Perley, D. A., Gal-Yam, A., Irani, I., & Zimmerman, E. 2023, TNSAN, 119, 1
Petropoulou, M., Kamble, A., & Sironi, L. 2016, MNRAS, 460, 44
Pledger, J. L., & Shara, M. M. 2023, ApJL, 953, L14
Pooley, D., & Lewin, W. H. G. 2002, IAUC, 8024, 2
Pooley, D., & Lewin, W. H. G. 2004, IAUC, 8390, 1
Pooley, D., Lewin, W. H. G., Fox, D. W., et al. 2002, ApJ, 572, 932
Qin, Y.-J., Zhang, K., Bloom, J., et al. 2024, MNRAS, 534, 271
Quataert, E., Fernández, R., Kasen, D., Klion, H., & Paxton, B. 2016, MNRAS, 458, 1214
Quataert, E., & Shiode, J. 2012, MNRAS, 423, L92
Ransome, C. L., Villar, V. A., Tartaglia, A., et al. 2024, ApJ, 965, 93
Reguitti, A., Pignata, G., Pastorello, A., et al. 2024, A&A, 686, A231
Reynolds, S. P., Williams, B. J., Borkowski, K. J., & Long, K. S. 2021, ApJ, 917, 55
Riess, A. G., Yuan, W., Macri, L. M., et al. 2022, ApJL, 934, L7
Ro, S., & Matzner, C. D. 2013, ApJ, 773, 79
Ruiz-Carmona, R., Sfaradi, I., & Horesh, A. 2022, A&A, 666, A82
Rybicki, G. B., & Lightman, A. P. 1979, Radiative Processes in Astrophysics (New York: Wiley)
Sarbadhicary, S. K., Badenes, C., Chomiuk, L., Caprioli, D., & Huizenga, D. 2017, MNRAS, 464, 2326
Sarmah, P. 2024, JCAP, 2024, 083
Schlegel, E. M. 1999, ApJL, 527, L85
Schlegel, E. M. 2001, ApJL, 556, L25
Schuster, M. T., Marengo, M., Hora, J. L., et al. 2009, ApJ, 699, 1423
Shrestha, M., DeSoto, S., Sand, D. J., et al. 2025, ApJL, 982, L32
Singh, A., Teja, R. S., Moriya, T. J., et al. 2024, ApJ, 975, 132
Smith, N. 2014, ARA&A, 52, 487
Smith, N., & Arnett, W. D. 2014, ApJ, 785, 82
Smith, N., Hinkle, K. H., & Ryde, N. 2009, AJ, 137, 3558
Smith, N., Pearson, J., Sand, D. J., et al. 2023, ApJ, 956, 46
Soderberg, A. M., Brunthaler, A., Nakar, E., Chevalier, R. A., & Bietenholz, M. F. 2010, ApJ, 725, 922
Soderberg, A. M., Chevalier, R. A., Kulkarni, S. R., & Frail, D. A. 2006, ApJ, 651, 1005
Soderberg, A. M., Kulkarni, S. R., Berger, E., et al. 2005, ApJ, 621, 908
Soraisam, M. D., Szalai, T., Van Dyk, S. D., et al. 2023, ApJ, 957, 64
Spitzer, L. 1978, Physical Processes in the Interstellar Medium (New York: Wiley)
Stepney, S. 1983, MNRAS, 202, 467
Strotjohann, N. L., Ofek, E. O., Gal-Yam, A., et al. 2021, ApJ, 907, 99
Szalai, T., Vinkó, J., Könyves-Tóth, R., et al. 2019, ApJ, 876, 19
Teja, R. S., Singh, A., Basu, J., et al. 2023, ApJL, 954, L12
Terreran, G., Jacobson-Galán, W. V., Groh, J. H., et al. 2022, ApJ, 926, 20
Thomas, B. P., Wheeler, J. C., Dwarkadas, V. V., et al. 2022, ApJ, 930, 57
Tiffany, C., Humphreys, R. M., Jones, T. J., & Davidson, K. 2010, AJ, 140, 339
Uno, S., Mitsuda, K., Inoue, H., et al. 2002, ApJ, 565, 419
Van Dyk, S. D., Srinivasan, S., Andrews, J. E., et al. 2024, ApJ, 968, 27
van Loon, J. T., Cioni, M. R. L., Zijlstra, A. A., & Loup, C. 2005, A&A, 438, 273
Vasylyev, S. S., Yang, Y., Filippenko, A. V., et al. 2023, ApJL, 955, L37
Waxman, E., Wasserman, T., Ofek, E., & Gal-Yam, A. 2025, ApJ, 978, 133
Willingale, R., Starling, R. L. C., Beardmore, A. P., Tanvir, N. R., & O'Brien, P. T. 2013, MNRAS, 431, 394
Wu, S., & Fuller, J. 2021, ApJ, 906, 3
Xiang, D., Mo, J., Wang, L., et al. 2024, Science China Physics, Mechanics & Astronomy, 67, 219514
Yadav, N., Ray, A., Chakraborti, S., et al. 2014, ApJ, 782, 30
Yamanaka, M., Fujii, M., & Nagayama, T. 2023, PASJ, 75, L27
Yaron, O., Perley, D. A., Gal-Yam, A., et al. 2017, NatPh, 13, 510
Zeng, H., Xin, Y., & Liu, S. 2019, ApJ, 874, 50
Zimmerman, E. A., Irani, I., Chen, P., et al. 2024, Natur, 627, 759